

All-atom Diffusion Transformers: Unified generative modelling of molecules and materials

Chaitanya K. Joshi^{1,2,*}, Xiang Fu¹, Yi-Lun Liao^{1,3,*}, Vahe Gharakhanyan¹, Benjamin Kurt Miller¹, Anuroop Sriram^{1,†}, Zachary W. Ulissi^{1,†}

¹Fundamental AI Research (FAIR) at Meta, ²University of Cambridge, ³MIT

*Work done during internship at FAIR, †Joint last author

Diffusion models are the standard toolkit for generative modelling of 3D atomic systems. However, for different types of atomic systems – such as molecules and materials – the generative processes are usually highly specific to the target system despite the underlying physics being the same. We introduce the All-atom Diffusion Transformer (ADiT), a unified latent diffusion framework for jointly generating both periodic materials and non-periodic molecular systems using the same model: (1) An autoencoder maps a unified, all-atom representations of molecules and materials to a shared latent embedding space; and (2) A diffusion model is trained to generate new latent embeddings that the autoencoder can decode to sample new molecules or materials. Experiments on MP20, QM9 and GEOM-DRUGS datasets demonstrate that jointly trained ADiT generates realistic and valid molecules as well as materials, obtaining state-of-the-art results on par with molecule and crystal-specific models. ADiT uses standard Transformers with minimal inductive biases for both the autoencoder and diffusion model, resulting in significant speedups during training and inference compared to equivariant diffusion models. Scaling ADiT up to half a billion parameters predictably improves performance, representing a step towards broadly generalizable foundation models for generative chemistry.

Correspondence: Chaitanya K. Joshi at chaitanya.joshi@cl.cam.ac.uk

Code: <https://github.com/facebookresearch/all-atom-diffusion-transformer>

In proceedings: 42nd International Conference on Machine Learning, PMLR 267, 2025



1 Introduction

Generative modelling of the 3D structure of atomic systems has the potential to revolutionize inverse design of new molecules and materials. The current state-of-the-art uses diffusion or flow matching models for tasks such as structure prediction (Abramson et al., 2024; Corso et al., 2023; Jiao et al., 2023) and conditional generation (Watson et al., 2023; Ingraham et al., 2023; Zeni et al., 2025) for biomolecules and materials, as well as for structure-based drug design (Schneuing et al., 2024).

All atomic systems share the same underlying physical principles that determine their 3D structure and interactions. However, we currently do not have a unified formulation of diffusion models across different types of atomic systems such as small molecules, biomolecules, crystals, and their combinations. Most diffusion models are highly specific to each type of system, and involve multi-modal generative processes on complex product manifolds of categorical and continuous data types. For example, de novo generation of small molecules is modelled as two independent diffusion processes for the atom types (categorical) and 3D coordinates (continuous) of a set of atoms (Hoogeboom et al., 2022). The denoiser model learns how atom types and 3D coordinates jointly evolve in order to sample new molecules but passes through unrealistic intermediate states during the denoising trajectory. Diffusion models for biomolecules treat groups of atoms as rigid bodies and add a third manifold (rotations) into the joint diffusion process (Yim et al., 2023b; Campbell et al., 2024). For crystals and materials, the diffusion process needs to additionally handle periodicity and operates on a joint manifold of atom types, fractional coordinates, lattice lengths, and lattice angles that together define the repeating unit cell (Xie et al., 2022; Miller et al., 2024).

In this paper, we pose the following question: *How can we build unified diffusion models that can generate both periodic materials and non-periodic molecular systems?*

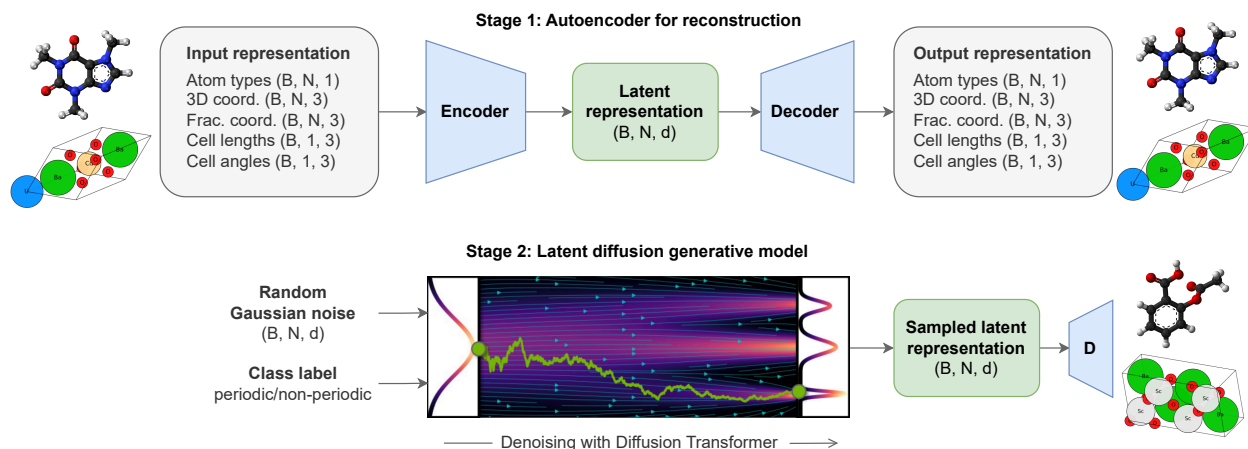


Figure 1 Unified generative modelling of molecules and materials with All-atom Diffusion Transformers. ADiT performs generative modelling of chemical systems in two stages: (1) A Variational Autoencoder (VAE) learns a shared latent space by reconstructing all-atom representations of both molecules (non-periodic) and crystals (periodic); and (2) A Diffusion Transformer (DiT) samples new latents from the shared distribution using classifier-free guidance, which are decoded to valid molecules or crystals using the VAE. Our unified latent diffusion framework enables transfer learning and avoids the complexity of multiple diffusion processes on categorical-continuous product manifolds used by equivariant diffusion models.

Our solution, the **All-atom Diffusion Transformer (ADiT)**, illustrated in [Figure 1](#), is a latent diffusion model based on two key ideas:

1. *All-atom unified latent representations:* We treat both periodic and non-periodic atomic systems as sets of atoms in 3D space and develop a unified representation with categorical and continuous attributes per atom. A Variational Autoencoder (VAE) ([Kingma and Welling, 2014](#)) embeds molecules and crystals into a shared latent space by training for all-atom reconstruction.
2. *Latent diffusion using Transformers:* We perform generative modelling in the latent space of the VAE encoder using a Diffusion Transformer (DiT) ([Rombach et al., 2022](#); [Peebles and Xie, 2023](#)). During inference, classifier-free guidance ([Ho and Salimans, 2022](#)) enables sampling new latents that can be reconstructed to valid molecules or crystals using the VAE decoder.

ADiTs can be trained jointly on both periodic and non-periodic atomic systems, demonstrating broad generalizability. Training a single unified model on the QM9 molecular and MP20 materials datasets leads to state-of-the-art performance in both domains, exceeding specialized equivariant diffusion models on physics-based validations. DFT calculations reveal that ADiTs generate stable, unique, and novel crystals at a 5-6% S.U.N. rate, a 25% improvement upon the 4-5% rates of previous methods. Joint training yields higher validity rates than QM9-only or MP20-only ADiT variants, demonstrating successful transfer learning between periodic and non-periodic systems. ADiTs also match or exceed state-of-the-art equivariant models on the GEOM-DRUGS dataset of molecules with hundreds of atoms.

ADiTs are highly scalable, achieving significant speedups in both training and inference compared to equivariant diffusion models. By using standard Transformers with minimal inductive biases for both the autoencoder and diffusion model, ADiTs can generate 10,000 samples in under 20 minutes on a single V100 GPU – an order of magnitude faster than baselines which take up to 2.5 hours on the same hardware. The practical efficiency of the DiT denoiser compared to equivariant networks allows us to scale ADiT to half a billion parameters while keeping data scale fixed. Our scaling law analysis demonstrates that generative modelling performance improves predictably with model size, suggesting further gains are possible through continued scaling.

All together, our work is the first to develop unified generative models for both periodic and non-periodic atomic systems, with state-of-the-art performance on both molecules and crystals. ADiTs represent a step towards broadly generalizable foundation models for generative chemistry.

2 All-atom Diffusion Transformers

Overview. We use latent diffusion (Rombach et al., 2022) to unify generative modelling across periodic and non-periodic atomic systems. Our approach consists of two stages: (1) A Variational Autoencoder (VAE) (Kingma and Welling, 2014) learns a shared latent space by jointly reconstructing all-atom representations of both molecules and materials; and (2) A Diffusion Transformer (Peebles and Xie, 2023) generates new samples from this latent space which can be decoded into valid molecules or crystals using classifier-free guidance (Ho and Salimans, 2022). Latent diffusion shifts the complexity of handling categorical and continuous attributes into the autoencoder, enabling a simplified and scalable generative process in latent space. We discuss how our contributions are contextualized w.r.t. related work in Appendix A.

2.1 Stage 1: Autoencoder for reconstruction

Unified representation of 3D atomic systems. All periodic and non-periodic atomic systems can be represented in a unified format as sets of atoms in 3D space (Duval et al., 2023). The key difference is that crystals require an additional periodic unit cell, while molecules have unbounded coordinates. A crystal or molecule with N atoms is represented as a multi-modal object:

$$\begin{aligned} \text{Atom types } \mathbf{A} &= \{a_i\}_{i=1}^N \in \mathbb{Z}^{1 \times N}, & \text{3D coords. } \mathbf{X} &= \{x_i\}_{i=1}^N \in \mathbb{R}^{3 \times N}, \\ \text{Fractional coords. } \mathbf{F} &= \{f_i\}_{i=1}^N \in [0, 1)^{3 \times N}, & \text{Unit cell/lattice } \mathbf{L} &= \{l_1, l_2, l_3\} \in \mathbb{R}^{3 \times 3}. \end{aligned}$$

The 3D coordinates \mathbf{X} are in nanometers, and the fractional coordinates \mathbf{F} are in the range $[0, 1)$. The lattice matrix \mathbf{L} represents a parallelepiped defining the shape of the repeating unit cell, and fractional coordinates are computed as the inverse of the unit cell matrix multiplied by the 3D coordinates: $\mathbf{F} = \mathbf{L}^{-1} \mathbf{X}$. We use Niggli reduction to uniquely determine the unit cell parameters for crystals (Grosse-Kunstleve et al., 2004). For non-periodic molecules, we set the unit cell parameters and fractional coordinates to null values ϕ .

VAE architecture. We use a Variational Autoencoder (VAE) to learn a shared latent representation of molecules and materials using a reconstruction objective. Given an input 3D atomic system $(\mathbf{A}, \mathbf{X}, \mathbf{F}, \mathbf{L})$, an encoder \mathcal{E} maps each atom’s attributes to a latent representation \mathbf{Z} :

$$\mathbf{Z} = \mathcal{E}(\mathbf{A}, \mathbf{X}, \mathbf{F}), \tag{1}$$

where $\mathbf{Z} = \{z_i\}_{i=1}^N \in \mathbb{R}^{d \times N}$ encodes information about the categorical atom type and continuous coordinates (unit cell parameters are encoded implicitly in the fractional coordinates). The decoder \mathcal{D} reconstructs the input atomic system from the latent embedding:

$$\mathbf{A}', \mathbf{X}', \mathbf{F}', \mathbf{L}' = \mathcal{D}(\mathbf{Z}). \tag{2}$$

We describe the pseudocode for VAE encoder and decoder operations in Algorithms 1 and 2, respectively. For the architecture of the encoder \mathcal{E} and decoder \mathcal{D} , we used the standard Transformer (Vaswani et al. (2017), `torch.nn.TransformerEncoder`) and learn symmetries via data augmentation. In Appendix D, we also ablated roto-translation equivariant VAEs based on Equiformer-V2 (Liao et al., 2024).

Algorithm 1: Pseudocode for VAE encoder \mathcal{E}	
Input: 3D atomic system $(\{a_i\}, \{x_i\}, \{f_i\}, \{l_1, l_2, l_3\})$	
Output: Latent representations $\{z_i\}$	
# Project inputs to d_{model}	
1. $h_i = \text{Embedding}(a_i)$	$h_i \in \mathbb{R}^{d_{\text{model}}}$
2. $h_i = h_i + \text{Linear}(\text{Swish}(\text{Linear}(x_i)))$	
3. $h_i = h_i + \text{Linear}(\text{Swish}(\text{Linear}(f_i)))$	
# Apply encoder network	
4. $\{h_i\} = \text{TransformerEncoder}(\{h_i\})$	
# Down-project to mean $\mu_{\mathbf{Z}}$ and std $\sigma_{\mathbf{Z}}$	
5. $\mu_{z_i} = \text{Linear}(h_i)$	$\mu_{z_i} \in \mathbb{R}^d$
6. $\log \sigma_{z_i} = \text{Linear}(h_i)$	$\sigma_{z_i} \in \mathbb{R}^d$
# Sample latents \mathbf{Z}	
7. $z_i = \mu_{z_i} + \sigma_{z_i} \odot \epsilon, \quad \epsilon \sim \mathcal{N}(0, 1)^d$	$z_i \in \mathbb{R}^d$

Algorithm 2: Pseudocode for VAE decoder \mathcal{D}	
Input: Latent representations $\{z_i\}$	
Output: 3D atomic system $(\{a'_i\}, \{x'_i\}, \{f'_i\}, \{l'_1, l'_2, l'_3\})$	
# Up-project latents to d_{model}	
1. $h_i = \text{Linear}(z_i)$	$h_i \in \mathbb{R}^{d_{\text{model}}}$
# Apply decoder network	
2. $\{h_i\} = \text{TransformerEncoder}(\{h_i\})$	
# Predict outputs	
3. $a'_i = \text{argmax}(\text{Linear}(h_i))$	$a'_i \in \mathbb{Z}$
4. $x'_i = \text{Linear}(h_i)$	$x'_i \in \mathbb{R}^3$
5. $f'_i = \text{Linear}(h_i)$	$f'_i \in \mathbb{R}^3$
6. $\{l'_1, l'_2, l'_3\} = \text{Linear}\left(\frac{1}{N} \sum_{i=1}^N h_i\right)$	$l' \in \mathbb{R}^3$

Reconstruction loss. We compute the loss for the predicted atom types \mathbf{A}' via cross-entropy:

$$\mathcal{L}_{\mathbf{A}} = \frac{1}{N} \sum_{i=1}^N \text{CrossEnt}(a_i, a'_i) . \tag{3}$$

For the predicted 3D coordinates \mathbf{X}' , we use the mean squared error (MSE) reconstruction loss after zero-centering both sets of coordinates:

$$\tilde{x}_i = x_i - \frac{1}{N} \sum_{i=1}^N x_i , \quad \tilde{x}'_i = x'_i - \frac{1}{N} \sum_{i=1}^N x'_i , \quad \mathcal{L}_{\mathbf{X}} = \frac{1}{3N} \sum_{i=1}^N \|\tilde{x}_i - \tilde{x}'_i\|^2 . \tag{4}$$

We compute the reconstruction loss for the predicted fractional coordinates \mathbf{F}' using MSE as well:

$$\mathcal{L}_{\mathbf{F}} = \frac{1}{3N} \sum_{i=1}^N \|f_i - f'_i\|^2 . \tag{5}$$

For the predicted lattice vectors \mathbf{L}' , we first convert to rotation-invariant lattice parameters: three side lengths of the unit cell $\mathbf{L}_l = \{a, b, c\} \in \mathbb{R}^{1 \times 3}$, and three internal angles between them $\mathbf{L}_a = \{\alpha, \beta, \gamma\} \in [60^\circ, 120^\circ]^{1 \times 3}$, as described in Miller et al. (2024). We then compute the MSE reconstruction loss between the predicted and ground truth lattice parameters:

$$\mathcal{L}_{\mathbf{L}_l} = \frac{1}{3} \left((a - a')^2 + (b - b')^2 + (c - c')^2 \right) , \tag{6}$$

$$\mathcal{L}_{\mathbf{L}_a} = \frac{1}{3} \left((\alpha - \alpha')^2 + (\beta - \beta')^2 + (\gamma - \gamma')^2 \right) . \tag{7}$$

Note that in $\mathcal{L}_{\mathbf{L}_l}$, we normalize the predicted and groundtruth lengths by the cube root of the number of atoms to account for the scaling of the unit cell with the number of atoms, following Xie et al. (2022). All angles are converted from degree to radians for numerical stability.

The autoencoder is trained with a weighted reconstruction loss to balance the relative magnitudes of the various losses. Depending on whether a training sample is periodic or non-periodic, we use different reconstruction loss weights:

$$\mathcal{L}_{\text{rec}} = \lambda_{\mathbf{A}} \mathcal{L}_{\mathbf{A}} + \lambda_{\mathbf{X}} \mathcal{L}_{\mathbf{X}} + \lambda_{\mathbf{F}} \mathcal{L}_{\mathbf{F}} + \lambda_{\mathbf{L}_l} \mathcal{L}_{\mathbf{L}_l} + \lambda_{\mathbf{L}_a} \mathcal{L}_{\mathbf{L}_a} , \quad \text{where} \tag{8}$$

	$\lambda_{\mathbf{A}}$	$\lambda_{\mathbf{X}}$	$\lambda_{\mathbf{F}}$	$\lambda_{\mathbf{L}_l}$	$\lambda_{\mathbf{L}_a}$
Periodic	1.0	0.0	10.0	1.0	10.0
Non-periodic	1.0	10.0	0.0	0.0	0.0

Thus, the overall loss for periodic crystals trains the model to reconstruct the atom types, fractional coordinates and lattice parameters while ignoring the predicted 3D coordinates. Similarly, the overall loss for non-periodic molecules trains the model to reconstruct the atom types and 3D coordinates while ignoring the predicted fractional coordinates and lattice parameters.

Regularization. We use three regularization techniques to learn robust, informative latent representations: (1) A bottleneck architecture with latent dimension d significantly smaller than the encoder/decoder hidden dimension d_{model} (e.g., $d = 8$ vs $d_{\text{model}} = 512$). (2) A per-channel KL divergence penalty $\lambda_{\text{KL}} \cdot D_{\text{KL}}(\mathcal{N}(\mathbf{Z}; \mu_{\mathbf{Z}}, \sigma_{\mathbf{Z}}) \parallel \mathcal{N}(0, 1)^d)$ added to equation 8, following Rombach et al. (2022). (3) Denoising training with 10% of atoms having their types masked and coordinates perturbed by $\mathcal{N}(0, 0.1)$ Gaussian noise. For non-equivariant encoders/decoders, we also randomly rotate and translate each sample during training to learn symmetries via data augmentation.

Decoding latents to atomic systems. During inference or sampling from the DiT, the desired output type (periodic/non-periodic) determines how we process the decoder outputs. The VAE decoder \mathcal{D} generates four attributes for each system: (1) atom types, (2) 3D coordinates, (3) fractional coordinates, and (4) lattice parameters. For non-periodic molecules, we only utilize the atom types and 3D coordinates, constructing the molecule via RDKit. For periodic crystals, we combine the atom types, fractional coordinates, and lattice parameters to build the crystal structure using PyMatGen. This split decoding strategy allows a single unified model to share information between both domains while still respecting their distinct geometric constraints, enabling effective transfer learning between periodic and non-periodic systems.

2.2 Stage 2: Latent diffusion generative model

Diffusion formulation. We use Gaussian diffusion or flow matching as our generative framework, which iteratively denoises latent samples from a base distribution into samples from a target distribution (Sohl-Dickstein et al., 2015; Song and Ermon, 2019; Ho et al., 2020; Lipman et al., 2023). Our formulation uses linear interpolation between a standard normal base distribution and the target distribution of VAE encoder latent representations of 3D atomic systems (we describe it in terms of flow matching, though both formulations are equivalent; see Gao et al. (2024)). Thus, the diffusion model is trained after training the first stage VAE.

Our model learns to generate a set of N latent representations $\mathbf{Z} = \{z_i\}_{i=1}^N$, where each latent $z \in \mathbb{R}^d$ encodes information about one atom’s type, coordinates and unit cell, which can be decoded to a valid 3D atomic system using the VAE decoder \mathcal{D} . During training, given an input 3D atomic system $(\mathbf{A}, \mathbf{X}, \mathbf{F}, \mathbf{L})$, we first encode it to a latent representation \mathbf{Z} using the VAE encoder \mathcal{E} . We denote \mathbf{Z} as $\mathbf{Z}^{(1)}$, a ‘clean’ training sample at time $t = 1$. We then sample a random initial latent $\mathbf{Z}^{(0)}$ at time $t = 0$ from a d -dimensional standard normal distribution $\mathcal{N}(0, 1)^d$, and perform zero-centering by subtracting the per-channel mean of $\mathbf{Z}^{(0)}$. We then use linear interpolation to construct a ‘noisy’ interpolated sample $\mathbf{Z}^{(t)}$ at a randomly sampled time step $t \sim \mathcal{U}(0, 1)$:¹

$$\mathbf{Z}^{(t)} = (1 - t) \mathbf{Z}^{(0)} + t \mathbf{Z}^{(1)}. \tag{9}$$

Thus, we can define a groundtruth conditional vector field $u_t(\mathbf{Z}^{(t)}|\mathbf{Z}^{(1)})$ along the path from the noisy latents $\mathbf{Z}^{(t)}$ at time step t to the clean latents $\mathbf{Z}^{(1)}$ as:

$$u_t(\mathbf{Z}^{(t)}|\mathbf{Z}^{(1)}) = \frac{\mathbf{Z}^{(1)} - \mathbf{Z}^{(t)}}{1 - t}. \tag{10}$$

Samples from the base distribution can be transformed to samples from the target distribution by integrating the vector field $u_t(\mathbf{Z}^{(t)}|\mathbf{Z}^{(1)})$ over time t .

The goal of conditional flow matching is to train a denoiser network \mathcal{F} to match this conditional vector field u_t . To do so, the denoiser takes as input the intermediate noisy latents $\mathbf{Z}^{(t)}$ at time step t and an additional class label c (described subsequently) to predict the final clean latents $\mathbf{Z}^{(1)}$:

$$\mathbf{Z}^{(1)} = \mathcal{F}(\mathbf{Z}^{(t)}, t, c). \tag{11}$$

The denoiser is trained by minimizing an MSE loss between the resulting predicted conditional vector field and the groundtruth conditional vector field:

$$\begin{aligned} \mathcal{L}_{\text{fm}} &= \frac{1}{N} \sum_{i=1}^N \left\| \frac{z_i^{(1)} - z_i^{(t)}}{1 - t} - \frac{z_i'^{(1)} - z_i'^{(t)}}{1 - t} \right\|^2, \\ &= \frac{1}{(1 - t)^2} \frac{1}{N} \sum_{i=1}^N \|z_i^{(1)} - z_i'^{(1)}\|^2. \end{aligned} \tag{12}$$

In practice, we follow Yim et al. (2023a) and clip the value of t at 0.9 to prevent numerical instability.

Denoiser architecture. As the denoiser network \mathcal{F} , we use a class-conditional Diffusion Transformer (DiT) (Peebles and Xie, 2023). The DiT largely follows a standard Transformer architecture with the conditioning information incorporated via adaptive layer norm with zero-initialization, which replaces all layer norm operations. For class conditioning, we use a binary embedding to denote whether the system being generated is periodic (crystal) or non-periodic (molecule). This conditioning allows the model to learn domain-specific features while sharing most parameters. During training, we apply class label dropout with 10% probability to enable classifier-free guidance during inference. We also incorporate self-conditioning (Yim et al., 2023b) where the denoiser’s prediction from the previous timestep is concatenated to the current input with 50% dropout probability during training. While we currently only condition on the periodic/non-periodic class label, the DiT architecture can incorporate additional conditioning signals like target properties or geometric

¹In practice, we set a minimum value for time step $t_{\text{min}} = 0.01$.

constraints to enable controlled generation. This represents a promising direction for future work in inverse design applications.

Data augmentation. The DiT denoiser is trained with data augmentation to learn roto-translational and periodic symmetries in the VAE’s latent space. During training, each input system coordinates are randomly rotated and translated, and then converted to latents via the frozen VAE encoder \mathcal{E} before being input to the DiT.

Sampling with classifier-free guidance. To generate new atomic systems from the trained diffusion model, we use classifier-free guidance (Ho and Salimans, 2022) to steer the sampling process. At each denoising step, we compute both a conditional prediction based on the periodic/non-periodic class label c and an unconditional prediction with null class label ϕ . The final prediction is a weighted combination of these using guidance scale γ , allowing control over how strongly the generation follows the class conditioning. The full sampling procedure is outlined in Algorithm 3. Starting from Gaussian noise $\mathbf{Z}^{(0)}$, we iteratively denoise using the DiT model \mathcal{F} for T steps. At each step, we perform Euler integration of the vector field to gradually transform the noisy latents towards the target distribution. While we currently use simple Euler integration for efficiency, adaptive ODE solvers could potentially improve performance (Ma et al., 2024). Finally, we decode the denoised latents $\mathbf{Z}^{(1)}$ to a valid 3D atomic system using the VAE decoder \mathcal{D} .

Algorithm 3: Pseudocode for DiT sampling

Input: Class label c , num. integration steps T , cfg. scale γ
Output: Generated sample $(\mathbf{A}, \mathbf{X}, \mathbf{F}, \mathbf{L})$

Sample initial noisy latents $\mathbf{Z}^{(0)}$ at $t = 0$

1. $\mathbf{Z}^{(0)} = \{z_i^{(0)} \sim \mathcal{N}(0, 1)^d\}$
2. $\Delta t = 1/T$ # Step size
- # Denoising loop
3. for t in linspace(0.0, 1.0, T):
4. $\mathbf{Z}'_{\text{cond}} = \mathcal{F}(\mathbf{Z}^{(t)}, t, c)$ # Conditional prediction
5. $\mathbf{Z}'_{\text{uncond}} = \mathcal{F}(\mathbf{Z}^{(t)}, t, \phi)$ # Unconditional prediction
- # Conditioning via classifier-free guidance
6. $\mathbf{Z}' = (1 - \gamma) \cdot \mathbf{Z}'_{\text{uncond}} + \gamma \cdot \mathbf{Z}'_{\text{cond}}$
- # Euler integration step
7. $\mathbf{Z}^{(t+\Delta t)} = \mathbf{Z}^{(t)} + \Delta t \cdot \frac{\mathbf{Z}' - \mathbf{Z}^{(t)}}{1-t}$
- # Decode latents to 3D atomic system (Algorithm 2)
8. $\mathbf{A}, \mathbf{X}, \mathbf{F}, \mathbf{L} = \mathcal{D}(\mathbf{Z}^{(1)})$

3 Experimental Setup

Datasets. For our main experiments, we train models on periodic crystals from MP20 and non-periodic molecules from QM9, representing two distinct domains of atomic systems. MP20 (Xie et al., 2022) contains 45,231 metastable crystal structures from the Materials Project (Jain et al., 2013), each with up to 20 atoms in its unit cell and spanning 89 different element types. QM9 (Wu et al., 2018) consists of 130,000 stable small organic molecules containing up to nine heavy atoms (C, N, O, F) along with hydrogens. We split the data following prior work (Xie et al., 2022; Hoogetboom et al., 2022) to ensure fair comparisons. We also include results on the GEOM-DRUGS dataset of 430,000 large organic molecules up to 180 atoms (Axelrod and Gomez-Bombarelli, 2022), as well as the QMOF dataset of 14,000 metal-organic framework structures (Rosen et al., 2021).

Training and hyperparameters. We sequentially train the first-stage VAE and then the second-stage DiT using AdamW optimizer with a constant learning rate $1e - 4$, no weight decay, and batch size of 256. We use exponential moving average (EMA) of DiT weights over training with a decay of 0.9999. Both models are trained to convergence for at most 5000 epochs up to 3 days on 8 V100 GPUs.

For the first-stage VAE, we use a standard Transformer as both encoder \mathcal{E} and decoder \mathcal{D} with hidden dimension $d_{\text{model}} = 512$, 8 attention heads, and 8 layers (51M parameters total). The latent dimension is set to $d = 8$ with KL regularization weight $\lambda_{\text{KL}} = 1e - 5$ and 10% denoising perturbation during training. For the second-stage DiT denoiser, we report results primarily using DiT-B configurations: hidden dimension

Table 1 Crystal generation results on MP20. We report validity, stability, uniqueness, and novelty rates for 10,000 sampled crystals. ADiT shows improved performance over diffusion baselines across all metrics. We see significant gains for compositional validity due to a single diffusion process in the latent space, as opposed to joint continuous and categorical diffusion for baselines. Joint training with both molecular and crystal data improves crystal generation performance over MP20-only models. (Stable: DFT $E^{\text{hull}} < 0.0$, metastable: DFT $E^{\text{hull}} < 0.1$, * denotes results from MatterGen-MP for 1024 sampled crystals, † denotes results we replicated using the same DFT setup as ADiT.)

Model	Validity Rate (%) \uparrow			Metastable	Stable	M.S.U.N.	S.U.N.
	Structure	Composition	Overall	rate (%) \uparrow	rate (%) \uparrow	rate (%) \uparrow	rate (%) \uparrow
MP20-only	CDVAE	100.00	86.70	-	-	1.6	-
	DiffCSP	100.00	83.25	-	-	5.0	3.3
	UniMat	97.2	89.4	-	-	-	-
	FlowMM	96.85	83.19	80.30	30.6 [†]	4.6 [†]	22.5 [†]
	FlowLLM	99.94	90.84	90.81	66.9 [†]	13.9 [†]	26.3 [†]
	MatterGen-MP	-	-	-	78*	13*	21*
	MP20-only ADiT	99.58	90.46	90.13	81.6	14.1	25.91
	Jointly trained ADiT	99.74	92.14	91.92	81.0	15.4	28.2

$d_{\text{model}} = 768$, 12 attention heads, 12 layers, and 130M parameters total. We also evaluate smaller DiT-S (32M parameters) and larger DiT-L (450M) variants.

Two key inference-time hyperparameters are the number of ODE integration steps T and the classifier-free guidance scale γ . We find $T = 500$ or 1000 with $\gamma = 1.0$ or 2.0 consistently works well for both molecules and crystals. Additional ablation studies comparing joint vs. dataset-specific training, architecture variants, regularization techniques, and inference settings are presented in [Appendix D](#).

Evaluation metrics. We evaluate the ability of ADiTs to sample valid and realistic molecules and crystals. Following prior work ([Xie et al., 2022](#); [Hoogeboom et al., 2022](#)), we sample 10,000 crystals and molecules each and compute validity, stability, uniqueness and novelty rates using density functional theory (DFT) for crystals as well as validity, uniqueness and Posebusters sanity checks ([Buttenschoen et al., 2024](#)) for molecules. Detailed descriptions of all evaluation metrics are provided in [Appendix B](#).

Baselines. We compare ADiT trained jointly on both QM9 and MP20 to molecule-only and crystal-only ADiT variants, as well as state-of-the-art baselines for both datasets. For crystal generation on MP20, we compare to: (1) three equivariant diffusion and flow matching-based models operating on multi-modal product manifolds: CDVAE ([Xie et al., 2022](#)), DiffCSP ([Jiao et al., 2023](#)), and FlowMM ([Miller et al., 2024](#)); (2) UniMat ([Yang et al., 2024](#)), a non-equivariant diffusion model which learns symmetries from data; (3) FlowLLM ([Sriram et al., 2024](#)), a two-stage framework which first finetunes the autoregressive Llama 2 language model on crystal structures ([Touvron et al., 2023](#); [Gruver et al., 2024](#)), and then trains FlowMM with samples from the language model as the base distribution and MP20 as the target distribution.

For molecule generation on QM9, we compare to: (1) Equivariant Diffusion ([Hoogeboom et al., 2022](#)), a roto-translationally equivariant diffusion model operating on a multi-modal product manifold; (2) GeoLDM ([Xu et al., 2023](#)), an alternative latent diffusion model using Equivariant Diffusion in the latent space of a roto-translationally equivariant autoencoder; (3) Symphony ([Daigavane et al., 2024](#)), an equivariant and autoregressive generative model that iteratively builds a molecule atom-by-atom.

4 Results

State-of-the-art crystals and molecule generation. Results for crystal generation in [Table 1](#) show that ADiTs generate high-quality crystals compared to baseline diffusion models, achieving improved performance across validity, stability, uniqueness, and novelty metrics for 10,000 sampled crystals, with significant gains for compositional validity due to a single diffusion process in the VAE latent space rather than joint continuous and categorical diffusion. For molecule generation, ADiTs achieve state-of-the-art performance on validity and uniqueness metrics across 10,000 sampled molecules, as shown in [Table 2\(a\)](#), while Posebusters sanity

Table 2 Molecule generation results on QM9. We report (a) validity and uniqueness rates, as well as (b) % pass rates on 7 sanity checks from Posebusters for 10,000 sampled molecules. ADiTs match or improve performance w.r.t. baselines, and sample physically realistic structures. Joint training with both molecular and crystal data improves molecular generation performance over QM9-only models. (* denotes models which explicitly generate hydrogen atoms.)

(a) Validity results				(b) PoseBusters results				
		Model	Validity (%) \uparrow	Unique (%) \uparrow	Test (% pass) \uparrow	Symphony	Eq. Diff.	ADiT
QM9-only		Equivariant Diffusion	97.50	96.71	Atoms connected	99.92	99.88	99.70
		Equivariant Diffusion*	91.90	98.69	Bond angles	99.56	99.98	99.85
		GeoLDM*	93.80	98.82	Bond lengths	98.72	100.00	99.41
		Symphony*	83.50	97.98	Ring flat	100.00	100.00	100.00
		QM9-only ADiT	96.02	97.76	Double bond flat	99.07	98.58	99.98
		QM9-only ADiT*	92.19	97.90	Internal energy	95.65	94.88	95.86
		Jointly trained ADiT	97.43	96.92	No steric clash	98.16	99.79	99.79
		Jointly trained ADiT*	94.45	97.82				

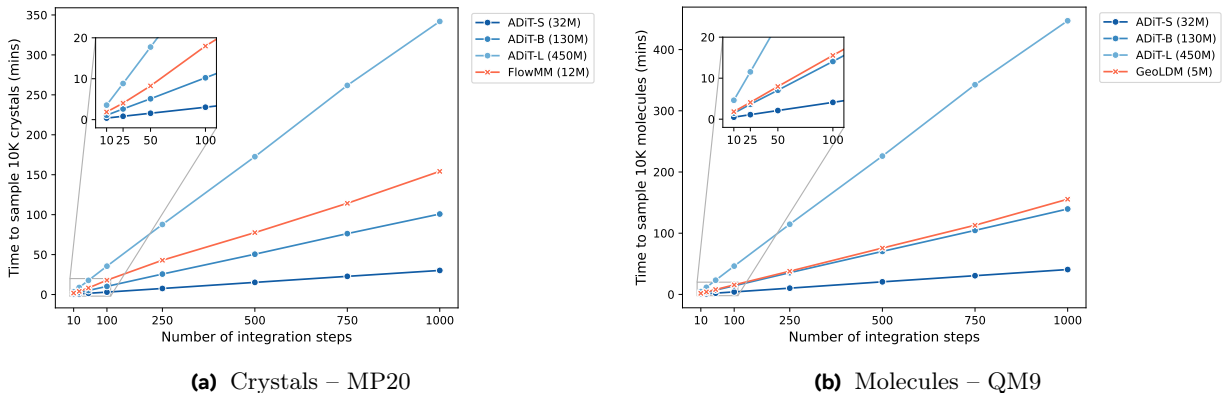


Figure 2 ADiTs are significantly faster than equivariant diffusion models. We plot the number of integration steps for ADiTs and equivariant diffusion models vs. time to generate 10,000 samples on a single V100 GPU. ADiTs scale significantly better with the number of integration steps compared to equivariant diffusion.

check metrics in Table 2(b) further confirm that ADiTs generate physically realistic molecular structures, matching or exceeding baseline models across measures like double bond flatness, reasonable internal energy and lack of steric clashes.

Joint training improves performance. Table 1 and Table 2 also show that jointly trained ADiTs (trained on both QM9 and MP20 together) exceed the performance of the MP20-only or QM9-only ADiTs for materials or molecules, respectively. Joint training improves validity and stability rates for both crystals and molecules, demonstrating effective transfer learning between periodic and non-periodic atomic systems. These results validate that ADiTs can effectively model diverse types of atomic systems within a single architecture.

Scaling up ADiT denoiser improves performance. In Figure 3, we see that generative modelling performance predictably improves as we scale the DiT denoiser from parameter counts of 32M (DiT-S) to 130M (DiT-B) all the way to 450M (DiT-L), even with our current modest dataset size of $\sim 130K$ total samples. The diffusion training loss and validity rates consistently improve with larger model sizes, showing a clear benefit from scale. Strong correlations between model size and performance metrics suggest further gains are possible from scaling both model size and data – Alexandria (2M inorganic crystals), ZINC (250M molecules), and the Protein Data Bank (200K biomolecular complexes) present promising opportunities for dataset scaling.

Speedup compared to equivariant diffusion. ADiTs achieve significant inference speedup compared to equivariant diffusion under the same hardware conditions, as shown in Figure 2. When generating 10,000 samples on a V100 GPU, ADiTs based on standard Transformers leads to better scaling with integration steps compared to FlowMM (Miller et al., 2024) for crystals and GeoLDM (Xu et al., 2023) for molecules, both of which use computationally intensive equivariant networks as denoisers. It is significantly more practical to scale up

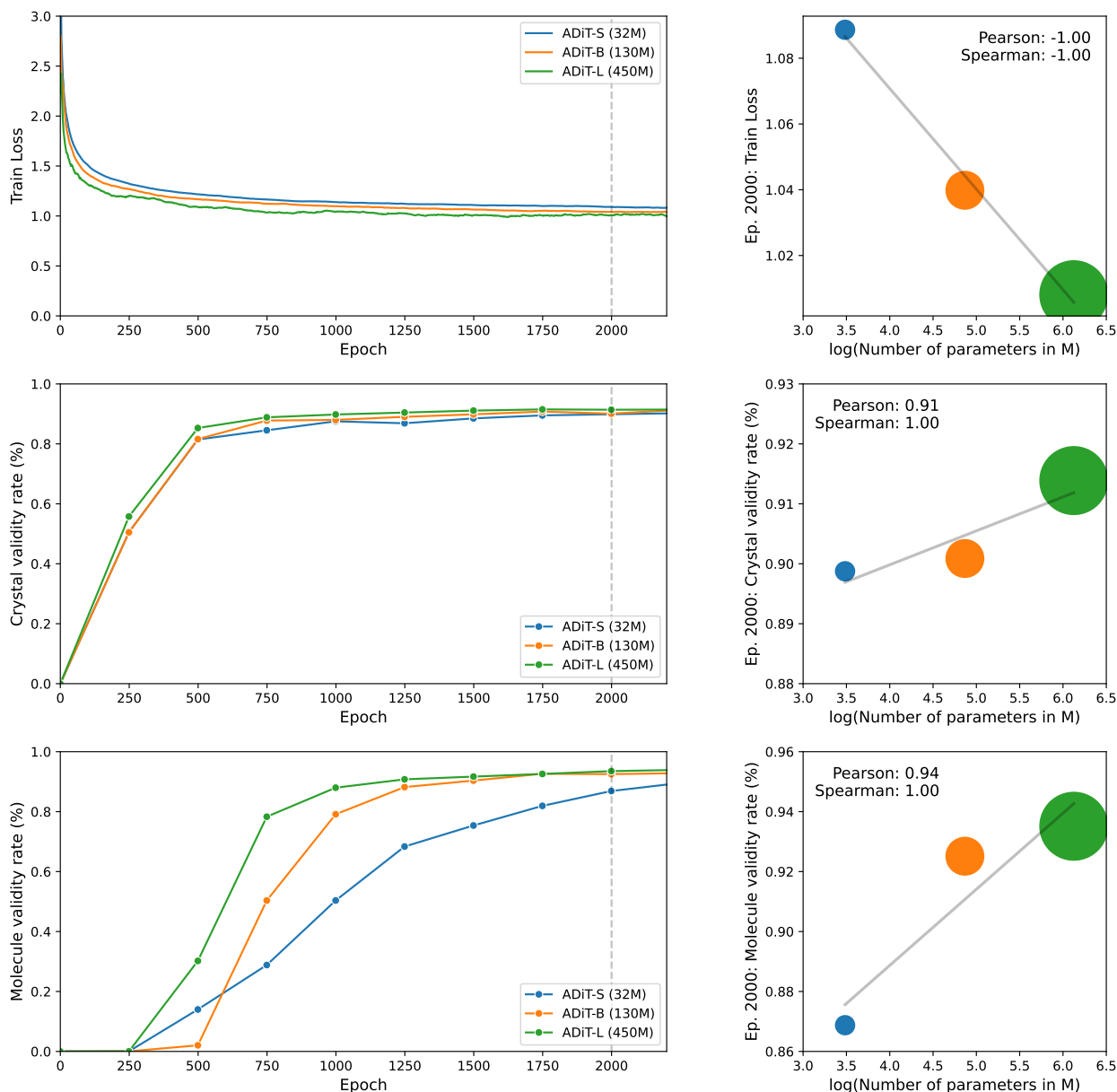


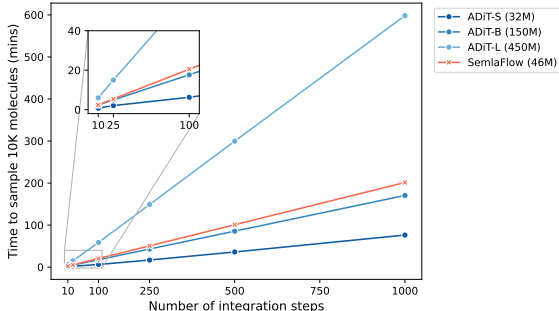
Figure 3 Scaling up ADiT improves performance. We show the effect of increasing the number of ADiT denoiser parameters on the training loss and generation validity rates. *Left:* training loss and validity rates vs. epochs. *Right:* Correlation plots for training loss and validity rates at epoch 2,000 vs. ADiT parameters (in Millions).

Transformers than equivariant networks, as seen by the faster inference speed of ADiT-B compared to $100\times$ smaller equivariant baselines.

Extension to larger GEOM-DRUGS molecules. To demonstrate the scalability of the ADiT architecture to larger systems, we experiment with the GEOM-DRUGS dataset of 430,000 molecules of up to 180 atoms. Our setup follows Vignac et al. (2023) and we compare to state-of-the-art equivariant diffusion (Le et al., 2024) and flow matching (Irwin et al., 2025) baselines. In Table 3, we see that ADiT is on par or better than equivariant models across validity and PoseBusters metrics (Buttenschoen et al., 2025). This is a notable result because ADiT is based on the standard Transformer architecture with minimal molecular inductive biases and, unlike equivariant baselines, does not explicitly predict atomic bonds.

Table 3 Molecule generation results on GEOM-DRUGS. *Left:* Validity, uniqueness and % pass rates on Posebusters for 10,000 sampled molecules (* PoseBusters results taken from [Buttenschoen et al. \(2025\)](#)). ADiT with minimal molecular inductive biases matches or exceeds state-of-the-art equivariant diffusion baselines, which explicitly predict atomic bonds. *Right:* We plot the number of integration steps for ADiTs and SemlaFlow vs. time to generate 10,000 molecules on a single A100 GPU. ADiTs scale favorably with the number of integration steps compared to SemlaFlow, a highly optimized equivariant diffusion model.

Metric (% pass) \uparrow	EQGAT-diff*	SemlaFlow*	ADiT
Validity	94.6	93.9	95.3
Uniqueness	100.0	100.0	100.0
Atoms connected	84.4	92.3	93.0
Bond angles	86.9	94.8	92.3
Bond lengths	87.0	94.6	92.5
Ring flat	87.0	94.9	95.4
Double bond flat	87.0	94.2	95.3
Internal energy	86.8	94.8	91.3
No steric clash	82.9	92.0	91.8
PoseBusters valid	59.7	87.5	85.3



Additional results, ablations, and visualizations. For additional results and ablation studies, including extensions to metal-organic framework (MOF) generation, see [Appendix C](#) and [Appendix D](#), respectively. In [Appendix E](#), we further analyze transfer learning in ADiT’s joint latent space via PCA and visualize some sampled crystals, molecules, and MOFs.

5 Discussions

Our work represents a significant step towards a broadly applicable foundation model for generative chemistry. We have introduced a unified latent diffusion framework for generating molecules and materials using a single model, and demonstrated the benefits of transfer learning from diverse atomic systems. The All-atom Diffusion Transformer (ADiT) obtains state-of-the-art performance in molecular generation using an architecture based primarily on standard Transformers with minimal inductive biases. This makes ADiT conceptually simpler and computationally more efficient than previous domain-specific approaches based on equivariant diffusion.

However, several limitations point to promising future directions. First, we currently use relatively small datasets for training, which may limit model generalization. Scaling to larger and more diverse datasets such as Alexandria and the Cambridge Structural Database for crystals, ZINC for small molecules, and the Protein Data Bank for biomolecular complexes could significantly improve performance and enable learning of broadly applicable chemical principles. Second, while we demonstrate success on small molecules and crystals of up to hundreds of atoms, we have not yet fully validated our approach on larger systems such as metal-organic frameworks or biomolecules containing thousands of atoms, though initial results for MOF generation are promising. Recent work on biomolecular structure prediction with AlphaFold3 ([Abramson et al., 2024](#)) demonstrates that simple Gaussian diffusion models with standard Transformers can effectively handle systems with thousands of atoms. Adapting ADiT to larger scales, while maintaining its unified representation across periodic and non-periodic systems, could enable powerful transfer learning capabilities – especially valuable for low-data domains. Finally, our current models only perform unconditional generation – extending to conditional generation based on experimental properties, motif scaffolding, or molecular infilling would enable practical inverse design applications in drug discovery, materials science, and beyond.

References

- Josh Abramson, Jonas Adler, Jack Dunger, Richard Evans, Tim Green, Alexander Pritzel, Olaf Ronneberger, Lindsay Willmore, Andrew J Ballard, Joshua Bambrick, et al. Accurate structure prediction of biomolecular interactions with alphafold 3. *Nature*, 2024.
- Simon Axelrod and Rafael Gomez-Bombarelli. Geom, energy-annotated molecular conformations for property prediction and molecular generation. *Scientific Data*, 2022.
- Ilyes Batatia, Philipp Benner, Yuan Chiang, Alin M Elena, Dávid P Kovács, Janosh Riebesell, Xavier R Advincula, Mark Asta, Matthew Avaylon, William J Baldwin, et al. A foundation model for atomistic materials chemistry. *arXiv preprint arXiv:2401.00096*, 2023.
- James Betker, Gabriel Goh, Li Jing, Tim Brooks, Jianfeng Wang, Linjie Li, Long Ouyang, Juntang Zhuang, Joyce Lee, Yufei Guo, et al. Improving image generation with better captions, 2023.
- Tim Brooks, Bill Peebles, Connor Holmes, Will DePue, Yufei Guo, Li Jing, David Schnurr, Joe Taylor, Troy Luhman, Eric Luhman, et al. Video generation models as world simulators. 2024.
- Martin Buttenschoen, Garrett M Morris, and Charlotte M Deane. Posebusters: Ai-based docking methods fail to generate physically valid poses or generalise to novel sequences. *Chemical Science*, 2024.
- Martin Buttenschoen, Yael Ziv, Garrett M Morris, and Charlotte Deane. An evaluation of unconditional 3d molecular generation methods. In *ICLR Workshop on Generative and Experimental Perspectives for Biomolecular Design*, 2025.
- Andrew Campbell, Jason Yim, Regina Barzilay, Tom Rainforth, and Tommi Jaakkola. Generative flows on discrete state-spaces: Enabling multimodal flows with applications to protein co-design. In *Forty-first International Conference on Machine Learning*, 2024.
- Alexander E Chu, Jinho Kim, Lucy Cheng, Gina El Nesr, Minkai Xu, Richard W Shuai, and Po-Ssu Huang. An all-atom protein generative model. *Proceedings of the National Academy of Sciences*, 2024.
- Gabriele Corso, Bowen Jing, Regina Barzilay, Tommi Jaakkola, et al. Diffdock: Diffusion steps, twists, and turns for molecular docking. In *International Conference on Learning Representations*, 2023.
- Xiaoliang Dai, Ji Hou, Chih-Yao Ma, Sam Tsai, Jialiang Wang, Rui Wang, Peizhao Zhang, Simon Vandenhende, Xiaofang Wang, Abhimanyu Dubey, et al. Emu: Enhancing image generation models using photogenic needles in a haystack. *arXiv preprint arXiv:2309.15807*, 2023.
- Ameya Daigavane, Song Eun Kim, Mario Geiger, and Tess Smidt. Symphony: Symmetry-equivariant point-centered spherical harmonics for 3d molecule generation. In *ICLR*, 2024.
- Daniel W Davies, Keith T Butler, Adam J Jackson, Jonathan M Skelton, Kazuki Morita, and Aron Walsh. Smact: Semiconducting materials by analogy and chemical theory. *Journal of Open Source Software*, 2019.
- Bowen Deng, Peichen Zhong, KyuJung Jun, Janosh Riebesell, Kevin Han, Christopher J Bartel, and Gerbrand Ceder. Chgnet as a pretrained universal neural network potential for charge-informed atomistic modelling. *Nature Machine Intelligence*, 2023.
- Prafulla Dhariwal and Alexander Nichol. Diffusion models beat gans on image synthesis. *Advances in neural information processing systems*, 2021.
- Alexandre Duval, Simon V Mathis, Chaitanya K Joshi, Victor Schmidt, Santiago Miret, Fragkiskos D Malliaros, Taco Cohen, Pietro Lio, Yoshua Bengio, and Michael Bronstein. A hitchhiker’s guide to geometric gns for 3d atomic systems. *arXiv preprint arXiv:2312.07511*, 2023.
- Patrick Esser, Sumith Kulal, Andreas Blattmann, Rahim Entezari, Jonas Müller, Harry Saini, Yam Levi, Dominik Lorenz, Axel Sauer, Frederic Boesel, et al. Scaling rectified flow transformers for high-resolution image synthesis. In *International Conference on Machine Learning*, 2024.
- Daniel Flam-Shepherd and Alán Aspuru-Guzik. Language models can generate molecules, materials, and protein binding sites directly in three dimensions as xyz, cif, and pdb files. *arXiv preprint arXiv:2305.05708*, 2023.
- Xiang Fu, Tian Xie, Andrew S. Rosen, Tommi S. Jaakkola, and Jake A. Smith. MOFDiff: Coarse-grained diffusion for metal-organic framework design. In *ICLR*, 2024.

- Ruiqi Gao, Emiel Hooeboom, Jonathan Heek, Valentin De Bortoli, Kevin P. Murphy, and Tim Salimans. Diffusion meets flow matching: Two sides of the same coin. 2024. <https://diffusionflow.github.io/>.
- Ralf W Grosse-Kunstleve, Nicholas K Sauter, and Paul D Adams. Numerically stable algorithms for the computation of reduced unit cells. *Acta Crystallographica Section A: Foundations of Crystallography*, 2004.
- Nate Gruver, Anuroop Sriram, Andrea Madotto, Andrew Gordon Wilson, C Lawrence Zitnick, and Zachary Ward Ulissi. Fine-tuned language models generate stable inorganic materials as text. In *The Twelfth International Conference on Learning Representations*, 2024.
- Charles Harris, Kieran Didi, Arian R Jamasb, Chaitanya K Joshi, Simon V Mathis, Pietro Lio, and Tom Blundell. Benchmarking generated poses: How rational is structure-based drug design with generative models? *arXiv preprint arXiv:2308.07413*, 2023.
- Jonathan Ho and Tim Salimans. Classifier-free diffusion guidance. *arXiv preprint arXiv:2207.12598*, 2022.
- Jonathan Ho, Ajay Jain, and Pieter Abbeel. Denoising diffusion probabilistic models. *Advances in neural information processing systems*, 2020.
- Emiel Hooeboom, Victor Garcia Satorras, Clément Vignac, and Max Welling. Equivariant diffusion for molecule generation in 3d. In *International conference on machine learning*, pages 8867–8887. PMLR, 2022.
- John B Ingraham, Max Baranov, Zak Costello, Karl W Barber, Wujie Wang, Ahmed Ismail, Vincent Frappier, Dana M Lord, Christopher Ng-Thow-Hing, Erik R Van Vlack, et al. Illuminating protein space with a programmable generative model. *Nature*, 2023.
- Ross Irwin, Alessandro Tibo, Jon Paul Janet, and Simon Olsson. Semlaflow—efficient 3d molecular generation with latent attention and equivariant flow matching. In *The 28th International Conference on Artificial Intelligence and Statistics*, 2025.
- Kevin M Jablonka. MOFChecker v0.9.6, 2023. <https://github.com/kjappelbaum/mofchecker>.
- Anubhav Jain, Shyue Ping Ong, Geoffroy Hautier, Wei Chen, William Davidson Richards, Stephen Dacek, Shreyas Cholia, Dan Gunter, David Skinner, Gerbrand Ceder, et al. Commentary: The materials project: A materials genome approach to accelerating materials innovation. *APL materials*, 2013.
- Rui Jiao, Wenbing Huang, Peijia Lin, Jiaqi Han, Pin Chen, Yutong Lu, and Yang Liu. Crystal structure prediction by joint equivariant diffusion. In *Thirty-seventh Conference on Neural Information Processing Systems*, 2023.
- Chaitanya Joshi. Transformers are graph neural networks. *The Gradient*, 2020.
- Chaitanya K Joshi, Cristian Bodnar, Simon V Mathis, Taco Cohen, and Pietro Lio. On the expressive power of geometric graph neural networks. In *International conference on machine learning*, 2023.
- John Jumper, Richard Evans, Alexander Pritzel, Tim Green, Michael Figurnov, Olaf Ronneberger, Kathryn Tunyasuvunakool, Russ Bates, Augustin Židek, Anna Potapenko, et al. Highly accurate protein structure prediction with alphafold. *Nature*, 2021.
- Diederik P Kingma and Max Welling. Auto-encoding variational bayes. In *International Conference on Learning Representations*, 2014.
- Tuan Le, Julian Cremer, Frank Noe, Djork-Arné Clevert, and Kristof T Schütt. Navigating the design space of equivariant diffusion-based generative models for de novo 3d molecule generation. In *The Twelfth International Conference on Learning Representations*, 2024.
- Yi-Lun Liao, Brandon M Wood, Abhishek Das, and Tess Smidt. Equiformerv2: Improved equivariant transformer for scaling to higher-degree representations. In *International Conference on Learning Representations*, 2024.
- Yaron Lipman, Ricky T. Q. Chen, Heli Ben-Hamu, Maximilian Nickel, and Matt Le. Flow matching for generative modeling. In *International Conference on Learning Representations*, 2023.
- Nanye Ma, Mark Goldstein, Michael S Albergo, Nicholas M Boffi, Eric Vanden-Eijnden, and Saining Xie. Sit: Exploring flow and diffusion-based generative models with scalable interpolant transformers. In *ECCV*, 2024.
- Karolis Martinkus, Jan Ludwiczak, Wei-Ching Liang, Julien Lafrance-Vanasse, Isidro Hotzel, Arvind Rajpal, et al. Abdiffuser: full-atom generation of in-vitro functioning antibodies. *Advances in Neural Information Processing Systems*, 2024.

- Benjamin Kurt Miller, Ricky TQ Chen, Anuroop Sriram, and Brandon M Wood. Flowmm: Generating materials with riemannian flow matching. In *Forty-first International Conference on Machine Learning*, 2024.
- Pedro O O Pinheiro, Joshua Rackers, Joseph Kleinhenz, Michael Maser, Omar Mahmood, Andrew Watkins, Stephen Ra, Vishnu Sresht, and Saeed Saremi. 3d molecule generation by denoising voxel grids. *Advances in Neural Information Processing Systems*, 36:69077–69097, 2023.
- Shyue Ping Ong, William Davidson Richards, Anubhav Jain, Geoffroy Hautier, Michael Kocher, Shreyas Cholia, Dan Gunter, Vincent L Chevrier, Kristin A Persson, and Gerbrand Ceder. Python materials genomics (pymatgen): A robust, open-source python library for materials analysis. *Computational Materials Science*, 2013.
- William Peebles and Saining Xie. Scalable diffusion models with transformers. In *International Conference on Computer Vision*, 2023.
- Janosh Riebesell, Rhys EA Goodall, Anubhav Jain, Philipp Benner, Kristin A Persson, and Alpha A Lee. Matbench discovery—an evaluation framework for machine learning crystal stability prediction. *arXiv preprint arXiv:2308.14920*, 2023.
- Robin Rombach, Andreas Blattmann, Dominik Lorenz, Patrick Esser, and Björn Ommer. High-resolution image synthesis with latent diffusion models. In *CVPR*, 2022.
- Andrew S Rosen, Shaelyn M Iyer, Debmalya Ray, Zhenpeng Yao, Alan Aspuru-Guzik, Laura Gagliardi, Justin M Notestein, and Randall Q Snurr. Machine learning the quantum-chemical properties of metal–organic frameworks for accelerated materials discovery. *Matter*, 2021.
- Victor Garcia Satorras, Emiel Hoogeboom, and Max Welling. E (n) equivariant graph neural networks. In *International conference on machine learning*. PMLR, 2021.
- Arne Schneuing, Charles Harris, Yuanqi Du, Kieran Didi, Arian Jamasb, Ilia Igashov, et al. Structure-based drug design with equivariant diffusion models. *Nature Computational Science*, 2024.
- Nima Shoghi, Adeesh Kolluru, John R. Kitchin, Zachary Ward Ulissi, C. Lawrence Zitnick, and Brandon M Wood. From molecules to materials: Pre-training large generalizable models for atomic property prediction. In *ICLR*, 2024.
- Jascha Sohl-Dickstein, Eric Weiss, Niru Maheswaranathan, and Surya Ganguli. Deep unsupervised learning using nonequilibrium thermodynamics. In *International conference on machine learning*, 2015.
- Yang Song and Stefano Ermon. Generative modeling by estimating gradients of the data distribution. *Advances in neural information processing systems*, 2019.
- Anuroop Sriram, Benjamin Kurt Miller, Ricky T. Q. Chen, and Brandon M. Wood. Flowllm: Flow matching for material generation with large language models as base distributions. In *NeurIPS*, 2024.
- Hugo Touvron, Louis Martin, Kevin Stone, Peter Albert, Amjad Almahairi, Yasmine Babaei, Nikolay Bashlykov, Soumya Batra, Prajjwal Bhargava, Shruiti Bhosale, et al. Llama 2: Open foundation and fine-tuned chat models. *arXiv preprint arXiv:2307.09288*, 2023.
- Arash Vahdat, Karsten Kreis, and Jan Kautz. Score-based generative modeling in latent space. *Advances in neural information processing systems*, 2021.
- Ashish Vaswani, Noam Shazeer, Niki Parmar, Jakob Uszkoreit, Llion Jones, Aidan N Gomez, Lukasz Kaiser, and Illia Polosukhin. Attention is all you need. *Advances in neural information processing systems*, 2017.
- Clement Vignac, Nagham Osman, Laura Toni, and Pascal Frossard. Midi: Mixed graph and 3d denoising diffusion for molecule generation. In *ECML PKDD*, 2023.
- Yuyang Wang, Ahmed AA Elhag, Navdeep Jaitly, Joshua M Susskind, and Miguel Angel Bautista. Swallowing the bitter pill: Simplified scalable conformer generation. In *International conference on machine learning*, 2024.
- Joseph L Watson, David Juergens, Nathaniel R Bennett, Brian L Trippe, Jason Yim, Helen E Eisenach, Woody Ahern, Andrew J Borst, Robert J Ragotte, Lukas F Milles, et al. De novo design of protein structure and function with rfdiffusion. *Nature*, 2023.
- Zhenqin Wu, Bharath Ramsundar, Evan N Feinberg, Joseph Gomes, Caleb Geniesse, Aneesh S Pappu, Karl Leswing, and Vijay Pande. Moleculenet: a benchmark for molecular machine learning. *Chemical science*, 2018.
- Tian Xie, Xiang Fu, Octavian-Eugen Ganea, Regina Barzilay, and Tommi S. Jaakkola. Crystal diffusion variational autoencoder for periodic material generation. In *International Conference on Learning Representations*, 2022.

- Minkai Xu, Alexander S Powers, Ron O Dror, Stefano Ermon, and Jure Leskovec. Geometric latent diffusion models for 3d molecule generation. In *International Conference on Machine Learning*, 2023.
- Sherry Yang, KwangHwan Cho, Amil Merchant, Pieter Abbeel, Dale Schuurmans, Igor Mordatch, and Ekin Dogus Cubuk. Scalable diffusion for materials generation. In *The Twelfth International Conference on Learning Representations*, 2024.
- Jason Yim, Andrew Campbell, Andrew YK Foong, Michael Gastegger, José Jiménez-Luna, Sarah Lewis, Victor Garcia Satorras, Bastiaan S Veeling, Regina Barzilay, Tommi Jaakkola, et al. Fast protein backbone generation with se (3) flow matching. *arXiv preprint arXiv:2310.05297*, 2023a.
- Jason Yim, Brian L Trippe, Valentin De Bortoli, Emile Mathieu, Arnaud Doucet, Regina Barzilay, and Tommi Jaakkola. Se (3) diffusion model with application to protein backbone generation. In *International Conference on Machine Learning*, pages 40001–40039. PMLR, 2023b.
- Claudio Zeni, Robert Pinsler, Daniel Zügner, Andrew Fowler, Matthew Horton, Xiang Fu, et al. Mattergen: a generative model for inorganic materials design. *Nature*, 2025.
- Lvmin Zhang, Anyi Rao, and Maneesh Agrawala. Adding conditional control to text-to-image diffusion models. In *Proceedings of the IEEE/CVF International Conference on Computer Vision*, 2023.

A Related Work

Generative models for molecules and materials. Diffusion models have emerged as the state-of-the-art for generative modelling of atomic systems, with applications to molecules, crystals, and biomolecules. For molecule generation, Equivariant Diffusion (Hoogeboom et al., 2022) pioneered roto-translationally equivariant diffusion on the multi-modal product manifold of atom types and 3D positions, while GeoLDM (Xu et al., 2023) introduced latent diffusion in the space of an equivariant autoencoder. Schneuing et al. (2024) extended equivariant diffusion to generate molecules conditioned on binding protein partners for structure-based drug design, while Corso et al. (2023) explored similar architectures for protein-small molecule docking. For crystal generation, state-of-the-art approaches use equivariant diffusion on product manifolds of atom types, 3D/fractional coordinates, and lattice parameters. Notable examples include CDVAE (Xie et al., 2022), DiffCSP (Jiao et al., 2023), and FlowMM (Miller et al., 2024). MatterGen (Zeni et al., 2025) demonstrated conditional diffusion for inverse design based on target material properties and symmetry space groups. Language models have also been used for generating molecules and crystals as textual representations (Flam-Shepherd and Aspuru-Guzik, 2023; Gruver et al., 2024).

Our work stands out as the first to develop unified generative models capable of sampling both periodic crystals and non-periodic molecular systems jointly. The closest work to ADiT in terms of diffusion formulation is AlphaFold3 (Abramson et al., 2024), which applies standard Transformers and Gaussian diffusion to generate all-atom biomolecular complex. However, their formulation is specific to structure prediction for biomolecules and only diffuses 3D atomic coordinates in Cartesian space. In contrast, our latent diffusion formulation is sufficiently general to work with both periodic and non-periodic systems, generating atom types, coordinates, as well as unit cell parameters unconditionally or with classifier-free guidance. Our emphasis on joint representations of molecules and crystals also aligns with recent work on general-purpose foundation models for molecular dynamics (Shoghi et al., 2024; Batatia et al., 2023). Similarly, our unified latent diffusion framework can potentially be scaled up with larger and more diverse chemical datasets towards foundation models for generative chemistry.

Latent diffusion models. Latent diffusion models (Vahdat et al., 2021; Rombach et al., 2022) propose to do diffusion in the latent space of an autoencoder instead of the raw input space of high-dimensional continuous signals such as pixels, and have been extremely successful for generating images, audio, and videos (Esser et al., 2024; Betker et al., 2023; Brooks et al., 2024). Latent diffusion is a more computationally efficient alternative to standard diffusion as the autoencoder’s latent space captures semantically meaningful features of the data, allowing for more efficient diffusion in a lower-dimensional space followed by reconstruction to the original data space. The original formulation was further improved by Diffusion Transformers (DiTs) (Peebles and Xie, 2023), which demonstrated that standard Transformers provide a highly scalable architecture for the denoiser network. Latent diffusion models can easily incorporate conditioning on additional information like class labels, text prompts, or infilling masks through classifier-based (Dhariwal and Nichol, 2021) and classifier-free guidance (Ho and Salimans, 2022) as well as finetuning (Zhang et al., 2023; Dai et al., 2023).

Our work is the first to leverage latent diffusion for jointly generating the complex multi-modal product of categorical and continuous data types that constitute 3D atomic systems. This allows us to shift the complexity of handling atom types, coordinates, and unit cell parameters into an autoencoder while performing the generative process in latent space with DiTs, which is simpler and more scalable than alternative multi-modal equivariant diffusion models.

Equivariance and generative modelling. Geometric Graph Neural Networks (Duval et al., 2023), particularly roto-translationally equivariant networks, have been used as denoisers in diffusion and flow matching approaches for generative modeling of 3D atomic systems. E(3)-Equivariant Graph ConvNets (Satorras et al., 2021) are widely used as denoisers for molecule (Hoogeboom et al., 2022; Xu et al., 2023; Schneuing et al., 2024) and crystal generation (Jiao et al., 2023; Miller et al., 2024). More expressive architectures, like higher-order tensor networks (Liao et al., 2024) and Invariant Point Attention (Jumper et al., 2021), have been applied to protein structure generation (Watson et al., 2023; Yim et al., 2023b) and protein-ligand docking (Corso et al., 2023).

However, equivariant networks are computationally expensive and harder to scale than standard Transformers in terms of data and model size. This is especially relevant for diffusion models, where denoisers typically process inputs as fully connected graphs to capture global structure (Joshi, 2020) and are iteratively run

hundreds of times during inference. Recent work has challenges the necessity of 3D inductive biases and equivariance for generative structure prediction tasks, showing that standard Transformers can achieve strong performance on biomolecular complexes (Abramson et al., 2024) and small molecule conformations (Wang et al., 2024; O Pinheiro et al., 2023). Non-equivariant models have also shown promising results for protein structure generation (Chu et al., 2024; Martinkus et al., 2024). In the same vein, our work leverages the simplicity and scalability of standard Transformers for generative modelling across both periodic and non-periodic 3D atomic systems, demonstrating that explicit equivariance and molecular inductive biases are not a strict requirement for generating valid and realistic atomic structures at scale.

B Evaluation Metrics

Crystal generation metrics. We follow the evaluation protocol established by Xie et al. (2022); Miller et al. (2024), where we sample 10,000 crystals and compute validity, stability, uniqueness, and novelty rates, defined as follows:

- Structural validity: % of crystals with all pairwise distances ≥ 0.5 and crystal volume ≥ 0.1 .
- Compositional validity: % of crystal compositions with charge neutrality and electronegativity balance according to SMOG (Davies et al., 2019).
- Overall validity: % of crystals which are both structurally and compositionally valid.
- Stability: % of crystals with DFT energy above hull < 0.0 eV/atom and no. of unique elements ≥ 2 . (We also report metastability as DFT energy above hull < 0.1 eV/atom and no. of unique elements ≥ 2 .)
- Stable & unique: % of stable crystals which are unique, as defined by an all-to-all comparison using Structure Matcher² from PyMatGen (Ong et al., 2013).
- Stable, unique & novel: % of stable, unique crystals which are novel, as defined by an all-to-all comparison to all crystals in MP-20 using Structure Matcher.

To compute the stability, uniqueness, and novelty rates, we follow Miller et al. (2024); Sriram et al. (2024): We first pre-relax the sampled crystals using a fast ML potential, CHGnet (Deng et al., 2023), and then perform DFT relaxation. We then determine the DFT energy above hull for the relaxed structures against the Matbench Discovery convex hull (Riebesell et al., 2023). Note that there is a lower bound on the number of completed DFT calculations due to memory or timeout errors.

Molecule generation metrics. We follow the evaluation protocol established by Hoogeboom et al. (2022); Daigavane et al. (2024), where we sample 10,000 molecules and compute validity and uniqueness rates as well as success rates for 7 sanity checks from Posebusters (Buttenschoen et al., 2024), as follows:

- Validity: % of molecules with canonical SMILES string found by RDKit.
- Uniqueness: % of unique SMILES among valid ones.
- All-atoms connected: % of molecules where there exists a path along bonds between all atoms.
- Reasonable bond angles/lengths: % of molecules where all angles/lengths are within 0.75 of the lower and 1.25 of the upper bounds determined by distance geometry.
- Aromatic rings flatness: % of molecules where All-atoms in aromatic rings with 5 or 6 members are within 0.25\AA of the closest shared plane molecule.
- Double bond flatness: % of molecules where All-atoms of aliphatic carbon-carbon double bonds and their four neighbours are within 0.25\AA of the closest shared plane.
- Reasonable internal energy: % of molecules where the calculated energy is no more than 100 times the average energy of an ensemble of 50 conformations generated for the input molecule.
- No internal steric clash: % of molecules where the interatomic distance between pairs of non-covalently bound atoms is above 0.8 of the distance geometry lower bound.

The validity and uniqueness metrics focus on whether the chemical composition of generated molecules can be processed by RDKit, while the Posebusters sanity checks evaluate the physical realism of the generated 3D structures across multiple criteria, from geometric constraints like bond lengths to energetic considerations (Harris et al., 2023).

²Structure Matcher checks if two periodic structures are equivalent, even if they are in different settings or have minor distortions.

C Additional Results

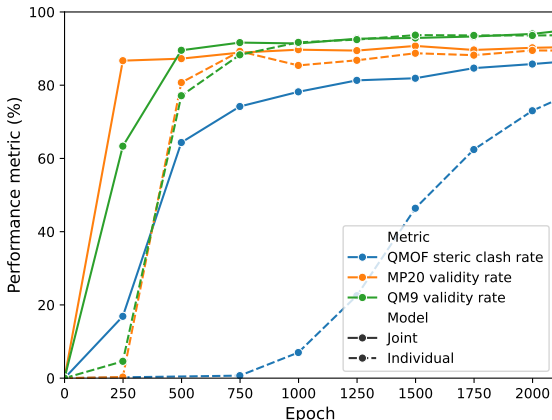
Extension to MOF generation.

Having established that ADiTs benefit from transfer learning to generate high-quality crystals and molecules, we challenged our architecture to generate metal-organic frameworks (MOFs), which represent a more complex class of hybrid materials with metal nodes connected by organic small molecule linkers. We trained ADiTs on an additional 14,000 MOFs of up to 150 atoms from the QMOF database (Rosen et al., 2021) alongside QM9 and MP20, using the same experimental settings and training for 10,000 epochs. We sampled 1,000 MOFs and evaluated their validity using 15 sanity checks from MOFChecker (Jablonka, 2023), including tests for: presence of metal/carbon/hydrogen atoms, atomic overlaps, over/undervalent carbons and nitrogens, missing hydrogens, and excessive partial charges.

Table 4 shows that QMOF-only trained ADiT achieves a 15% overall validity rate for MOF generation, which decreases to 10% with joint training on molecules, crystals, and MOFs simultaneously. However, the jointly trained model takes significant time to train and did not fully converge, suggesting that further improvements in MOF generation may be possible with larger models trained for longer. Comparing validity rates for joint vs. dataset-specific ADiTs shows that the joint model benefits from transfer learning across molecules, crystals, and MOFs, achieving high validity rates earlier in training. Notably, the joint model achieves high validity rates of 91% for crystals and 95% for molecules, matching our best dataset-specific models and being able to additionally generate MOFs. While not directly comparable, models specialized for MOF such as MOFDiff (Fu et al., 2024) are trained on large synthetic dataset of 300,000 MOFs and achieve 30% validity rates based on MOFChecker *after* DFT relaxation of generated MOFs. Our results are reported without DFT relaxation.

Table 4 Metal-organic framework generation results. *Left:* We report sanity checks from MOFChecker for 1,000 sampled MOFs, trained on QMOF-only as well as jointly with QM9 and MP20. (\uparrow/\downarrow indicate higher/lower is better, respectively.) *Right:* Jointly trained and dataset-specific ADiT validity rates vs. epochs. The joint model benefits from transfer learning and requires fewer epochs per dataset to start generating valid samples.

Test (%)	QMOF ADiT	Joint ADiT
Has carbon \uparrow	100.0	100.0
Has hydrogen \uparrow	99.6	100.0
Has atomic overlap \downarrow	8.3	10.8
Has overcoord. C \downarrow	23.6	34.3
Has overcoord. N \downarrow	1.5	1.6
Has overcoord. H \downarrow	1.0	3.6
Has undercoord. C \downarrow	60.0	72.1
Has undercoord. N \downarrow	39.1	39.9
Has undercoord. rare earth \downarrow	0.4	0.8
Has metal \uparrow	100.0	99.4
Has lone molecule \downarrow	72.9	83.2
Has high charge \downarrow	0.9	2.5
Has suspicious terminal oxo \downarrow	2.6	5.8
Has undercoord. alkali \downarrow	1.0	6.4
Has geom. exposed metal \downarrow	7.0	9.6
Validity rate (all passed) \uparrow	15.7	10.2



Histograms from DFT validation.

In Figure 4, we show histograms of DFT energy above hull, formation energy, and number of unique elements per crystal for 10,000 generated crystals from ADiT, FlowMM, and FlowLLM compared to the MP20 training distribution. ADiT generates more thermodynamically stable crystals than prior models, as shown by the larger proportion of samples with DFT energy above hull below 0.0 eV/atom. The distribution of DFT formation energies and number of unique elements per crystal from ADiT samples more closely matches the MP20 training data compared to FlowMM and FlowLLM baselines, suggesting that ADiT better captures the underlying physical and chemical constraints of stable crystal structures. Note that we ran DFT calculations for all model samples under identical hardware and settings to ensure fair comparison.

Histogram of spacegroups.

In Figure 5, we show the distribution of spacegroups for 10,000 generated crystals from ADiT, FlowMM, FlowLLM and the MP20 distribution. Diffusion-based models (ADiT and FlowMM) tend to over sample crystals with P1 spacegroup, which represents the lowest symmetry group, likely due to

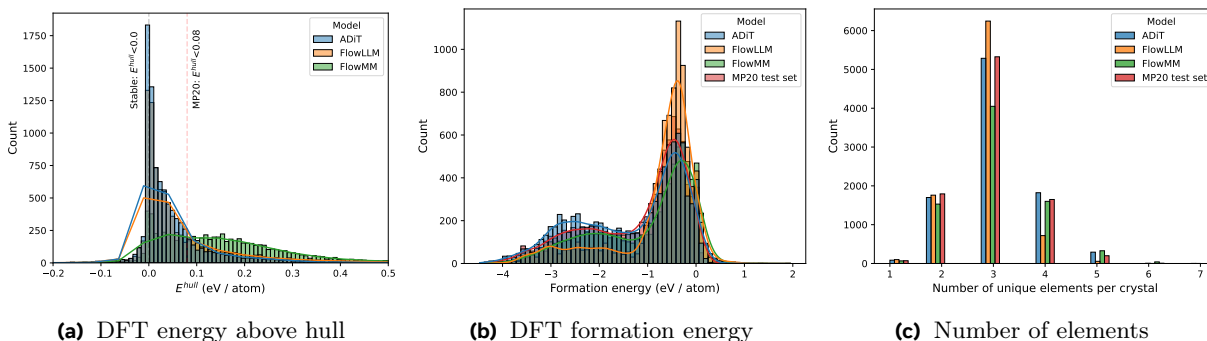


Figure 4 Histograms from DFT validation of 10,000 generated crystals. ADiT is more likely to generate stable crystals with DFT energy above hull <0.0 eV/atom compared to prior models. Samples from ADiT most closely follow the distributions for DFT formation energy and number of unique elements per crystal from MP20.

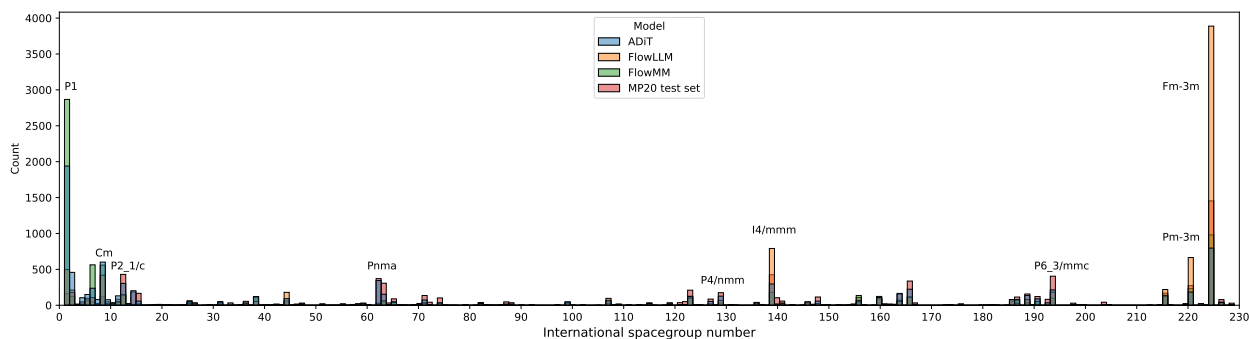


Figure 5 Histogram of spacegroups for 10,000 generated crystals. Diffusion-based ADiT and FlowMM tend to over sample crystals with P1 spacegroup compared to the MP20 training distribution. FlowLLM, an autoregressive language, tends to over sample crystals with Fm-3m, Pm-3m, and I4/mmm spacegroups.

their local, step-wise denoising process. In contrast, FlowLLM, an autoregressive language model, tends to over sample spacegroups like Fm-3m, Pm-3m, and I4/mmm compared to the training data. While it would be straightforward to control the distribution of spacegroups generated by ADiT through classifier-free guidance conditioning, we leave this for future work since our current focus is on unconditional generation of diverse atomic systems.

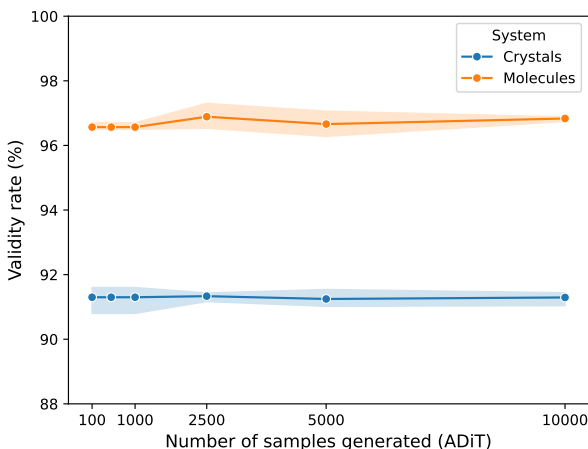
SUN rate and scaling ADiT. In Table 5, we observe that the combined stability, uniqueness, and novelty (S.U.N.) rate for crystal generation decreases as we scale up the DiT denoiser from DiT-S (32M) to DiT-L (450M). While stability and uniqueness rates increase with model size, the S.U.N. rate decreases due to the larger model’s greater capacity to memorize the small MP20 training dataset of 27K crystals. This suggests that larger models may be more prone to generating duplicate or near-duplicate samples, which we plan to address by training on larger and more diverse datasets in future work. For crystals, the Alexandria dataset of inorganic crystals and the Crystallography Open Database of organic crystals present promising opportunities for scaling up. Notably, ADiT-S trained on MP20-only achieves a S.U.N. rate of 6.5%, representing a significant improvement over previously published results from FlowMM (2.8%) and FlowLLM (4.7%). This demonstrates that even our smallest model variant substantially advances the state-of-the-art for crystal generation.

Sensitivity of validity rate to number of samples and random seed. In Figure 6a, we plot the validity rates for crystal and molecule generation as we increase the number of samples from 100 to 10,000 for 3 different random seeds. We observe that the validity rates generally converge and are stable across random seeds after sampling over 5,000 crystals or molecules.

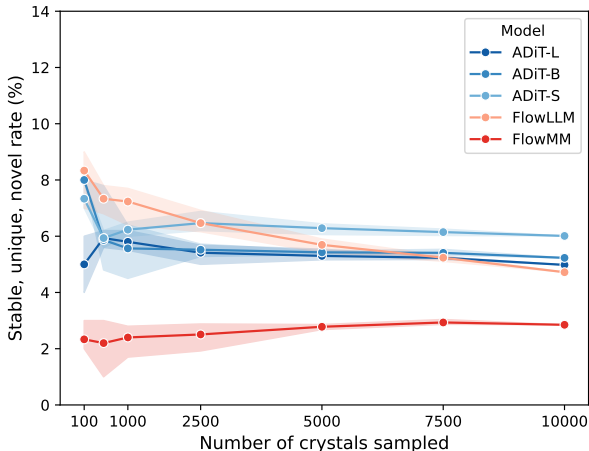
Sensitivity of S.U.N. rate to number of samples. In Figure 6b, we plot the S.U.N. (stability, uniqueness, and novelty) rates for crystal generation as we increase the number of samples from 100 to 10,000 across 3 different random seeds. The S.U.N. rates converge after approximately 5,000 samples for diffusion-based methods like

Table 5 Impact of scaling on stability, uniqueness, and novelty rates for 10,000 generated crystals. We find that stability rate as well as stability & uniqueness rate increase as we increase the number of model parameters for ADiT from 32M to 450M. However, larger ADiT models have greater capacity to memorise the small MP20 training dataset of 27K crystals, resulting in decrease in the combined stability, uniqueness, & novelty rate. ADiT-S trained on MP20-only achieves a S.U.N. rate of 6.5%, representing a significant improvement over previously published state-of-the-art models which attained S.U.N. rates up to 4.7%.

Model	Stability ($E^{\text{hull}} < 0.0$)			Metastability ($E^{\text{hull}} < 0.1$)		
	S (%) \uparrow	S.U. (%) \uparrow	S.U.N. (%) \uparrow	M.S (%) \uparrow	M.S.U. (%) \uparrow	M.S.U.N. (%) \uparrow
MP20-only ADiT-S (32M)	12.8	11.8	6.5	71.1	64.9	38.1
MP20-only ADiT-B (130M)	14.1	12.5	4.7	81.6	67.3	25.9
Joint ADiT-S (32M)	12.6	11.4	6.0	71.9	64.7	37.7
Joint ADiT-B (130M)	15.4	13.4	5.3	81.0	70.2	28.2
Joint ADiT-L (450M)	15.5	13.5	5.0	82.5	70.9	27.9



(a) Validity rates are consistent across random seeds.



(b) S.U.N. rates converge after 5,000 samples.

Figure 6 Consistency of validity and S.U.N. rates as we increase number of samples. We plot the validity and S.U.N. rates vs. number of sampled crystals or molecules. Error bars indicate 95% confidence interval across three different random seeds. Metrics are generally stable across seeds and converge after sampling over 5,000 crystals or molecules.

ADiT and FlowMM. In contrast, autoregressive models like FlowLLM show higher variance in S.U.N. rates, likely due to more frequent generation of duplicate crystals during low-temperature sampling.

D Ablation Study

Table 7 and Table 6 presents ablation studies as well as aggregated benchmarks for various configurations of ADiT’s latent diffusion model and autoencoder, respectively. Key takeaways are highlighted below. Note that, unless otherwise stated, results in the main paper are reported for jointly trained ADiT-B which uses DiT-B denoiser, standard Transformer encoder and decoder, latent dimension $d = 8$, and KL regularization weight $\lambda_{\text{KL}} = 1e - 5$.

Joint vs. dataset-specific training Joint training of the autoencoder to embed both molecules and crystals into a shared latent space achieves similar or better reconstruction performance compared to dataset-specific training, as shown in Table 6 (rows 3, 6, 10). The benefits of joint training are most evident in generative modelling performance – samples from the joint model have higher validity rates for both crystals and molecules compared to dataset-specific models, demonstrating effective transfer learning between periodic and non-periodic atomic systems (Table 7, rows 12, 16, 20). These results provide strong evidence that ADiTs can successfully unify the modelling of both periodic and non-periodic atomic systems within a single architecture, without compromising performance on either domain.

Denoiser architecture The DiT denoiser is a standard Transformer with key hyperparameters including the hidden dimension d_{model} , number of attention heads, and number of layers. Scaling up the DiT denoiser from DiT-S (32M parameters, $d_{\text{model}} = 384$, 6 heads, 12 layers) to DiT-B (150M, $d_{\text{model}} = 768$, 12 heads, 12 layers) and DiT-L (450M, $d_{\text{model}} = 1024$, 24 heads, 24 layers) consistently improves generative performance, as shown in Table 7 (rows 12, 16, 20). We have additionally performed scaling law analysis for the training loss and validity rates in Figure 3, seeing strong correlations between model size and performance metrics. In Figure 6b, we further see that S.U.N. rates for larger models are better than smaller models, further confirming the benefits of scaling up the DiT denoiser.

Autoencoder architecture For the architecture of the autoencoder’s encoder and decoder, we explored both roto-translation equivariant as well as non-equivariant VAEs. For the equivariant VAE variant, the encoder is Equiformer-V2 (Liao et al., 2024) and the decoder is an equivariant feedforward network adapted from output heads in the Equiformer-V2 codebase. We selected Equiformer-V2 as it is theoretically expressive (Joshi et al., 2023) and has state-of-the-art performance across diverse 3D atomic systems. As input to the Equiformer-V2 encoder, we use spherical harmonic embeddings of displacement vectors as edge features and exclude the 3D coordinates in Algorithm 1, line 2, from the initial features $\{h_i\}$ as a result. The initial features $\{h_i\}$ are used as the $L = 0$ scalar component of the initial spherical tensor features of Equiformer-V2. The rest of the pseudocode in Algorithms 1 and 2 remains the same.

As shown in Table 6 (rows 1-4 and 5-8), the choice of autoencoder architecture has noticeable impact on reconstruction performance. Standard Transformers generally outperform Equiformer-V2 for both crystals and molecules, achieving higher match rates (% of test set samples where the reconstructed structure matches the groundtruth, as determined by PyMatGen’s StructureMatcher/MoleculeMatcher). More importantly, the latent space learned by standard Transformers proved more suitable for the latent diffusion process compared to Equiformer-V2’s equivariant latent space, leading to substantially better generative performance in terms of validity rates, particularly for crystals (Table 7, rows 1-4 and 5-8).

Autoencoder regularization As shown in Table 6 (rows 9-12), increasing the latent dimension and reducing the KL regularization weight generally improved autoencoder reconstruction performance by lowering RMSD values which measure the average distance between the reconstructed and groundtruth structures. These improvements in reconstruction quality translated to better generative performance, with higher validity rates for both crystals and molecules at larger latent dimensions and lower KL weights (see Table 7, rows 9-12).

Sampling hyperparameters. Classifier-free guidance scale and number of integration steps are important hyperparameters for inference-time tuning. In Figure 7, we show a grid search over guidance scales $\gamma \in \{1.0, 2.0, 3.0, 4.0, 6.0\}$ and integration steps $T \in \{10, 50, 100, 250, 500, 1000\}$, finding that different combinations may be optimal for crystals vs. molecule generation. For each entry in Table 7, we have reported results for T and γ which obtain the highest validity rates. $T = 500$ or 1000 with $\gamma = 1.0$ or 2.0 tends to work well across both molecules and crystals.

Table 6 Autoencoder ablation study. We report match rate (computed with StructureMatcher or MoleculeMatcher from PyMatGen) and RMSD between the reconstructed and groundtruth structures for MP20 crystals and QM9 molecules.

Train Set	Autoencoder hyperparameters			Crystals – MP20		Molecules – QM9	
	Encoder	Latent	KL	Match Rate (%) \uparrow	RMSD (\AA) \downarrow	Match Rate (%) \uparrow	RMSD (\AA) \downarrow
MP20	Transformer	4	0.0001	85.50	0.0598	-	-
MP20	Equiformer-V2	4	0.0001	81.70	0.1652	-	-
MP20	Transformer	8	0.0001	84.50	0.0502	-	-
MP20	Equiformer-V2	8	0.0001	88.90	0.0296	-	-
QM9	Transformer	4	0.0001	-	-	97.20	0.0747
QM9	Equiformer-V2	4	0.0001	-	-	96.20	0.0765
QM9	Transformer	8	0.0001	-	-	96.50	0.0823
QM9	Equiformer-V2	8	0.0001	-	-	96.20	0.0746
Joint	Transformer	4	0.0001	88.30	0.0471	96.60	0.0785
Joint	Transformer	4	0.00001	88.50	0.0468	98.50	0.0524
Joint	Transformer	8	0.0001	88.60	0.0269	96.60	0.0760
Joint	Transformer	8	0.00001	88.60	0.0239	97.00	0.0399

Table 7 Latent diffusion model ablation study. We report validity rates for 10,000 generated crystals or molecules.

Train Set	Diffusion Denoiser	Autoencoder hyperparameters			Crystals – MP20			Molecules – QM9	
		Encoder	Latent	KL	Structure Valid (%) \uparrow	Composition Valid (%) \uparrow	Overall Valid (%) \uparrow	Validity (%) \uparrow	Validity* (%) \uparrow
MP20	DiT-S	Transformer	4	0.0001	98.90	89.19	88.19	-	-
MP20	DiT-S	Equiformer-V2	4	0.0001	91.74	81.03	74.43	-	-
MP20	DiT-S	Transformer	8	0.0001	99.58	90.46	90.13	-	-
MP20	DiT-S	Equiformer-V2	8	0.0001	99.26	86.09	85.50	-	-
QM9	DiT-S	Transformer	4	0.0001	-	-	-	95.94	92.19
QM9	DiT-S	Equiformer-V2	4	0.0001	-	-	-	95.36	91.37
QM9	DiT-S	Transformer	8	0.0001	-	-	-	96.02	91.58
QM9	DiT-S	Equiformer-V2	8	0.0001	-	-	-	96.24	91.47
Joint	DiT-S	Transformer	4	0.0001	98.21	91.05	89.38	96.90	93.47
Joint	DiT-S	Transformer	4	0.00001	98.74	90.74	89.60	96.40	91.85
Joint	DiT-S	Transformer	8	0.0001	99.66	91.07	90.76	96.85	93.33
Joint	DiT-S	Transformer	8	0.00001	99.67	91.25	90.93	96.36	92.06
Joint	DiT-B	Transformer	4	0.0001	99.00	91.23	90.29	97.33	94.45
Joint	DiT-B	Transformer	4	0.00001	99.51	90.73	90.29	97.04	94.06
Joint	DiT-B	Transformer	8	0.0001	99.67	91.60	91.32	95.30	89.85
Joint	DiT-B	Transformer	8	0.00001	99.74	92.14	91.92	97.43	93.99
Joint	DiT-L	Transformer	4	0.0001	99.31	90.92	90.29	97.80	94.67
Joint	DiT-L	Transformer	4	0.00001	99.43	90.84	90.31	96.71	92.78
Joint	DiT-L	Transformer	8	0.0001	99.75	92.17	91.92	96.11	91.45
Joint	DiT-L	Transformer	8	0.00001	99.66	91.42	91.14	97.79	95.01

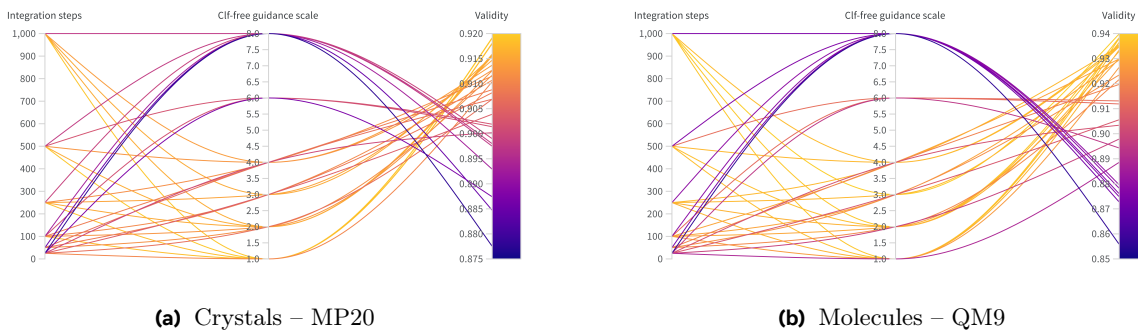


Figure 7 Tuning inference hyperparameters for best performance. Best generative modelling results for crystals and molecules are achieved with different classifier-free guidance scales γ and number of integration steps T . $T = 500$ or 1000 with $\gamma = 1.0$ or 2.0 tends to work well across both molecules and crystals.

E Visualizations

PCA visualization of shared latent space. In Figure 8, we plot the first two PCA principal components of 100 random samples each from the MP20 and QM9 validation set, as well as 100 generated crystals and 100 generated molecules sampled from ADiT. We observe that the joint latent space shows distinct clusters between molecules and crystals, with tighter clustering for molecules and more spread for crystals, reflecting the greater diversity of elements and local geometric environments in periodic crystal structures.

Next, we plot the same PCA but only keeping atoms of carbon, nitrogen, oxygen, and fluorine in Figure 9. These atoms appear in both QM9 molecules and MP20 crystals, allowing us to analyze how their representations compare across periodic and non-periodic systems. The visualization reveals clear patterns: principal component 1 primarily distinguishes between molecules (clustered between -2 and 2) and crystals, while principal component 2 correlates with atom type. Most notably, oxygen atoms show similar latent representations whether they appear in molecules or crystals, suggesting ADiT’s latent space captures fundamental chemical properties that transfer across both domains. This shared representation of oxygen, a key element in both datasets, may help explain ADiT’s successful joint learning and transfer between periodic and non-periodic systems.

Generated crystals, molecules, and MOFs. In Figure 10, Figure 11, and Figure 12, we show samples of generated crystals, molecules, and MOFs from ADiT, respectively. The generated crystals exhibit diverse spacegroups and compositions, while the generated molecules show a wide range of chemical structures and conformations. These visualizations demonstrate that the jointly trained ADiT model successfully generates high-quality and chemically diverse atomic systems in both periodic and non-periodic domains.

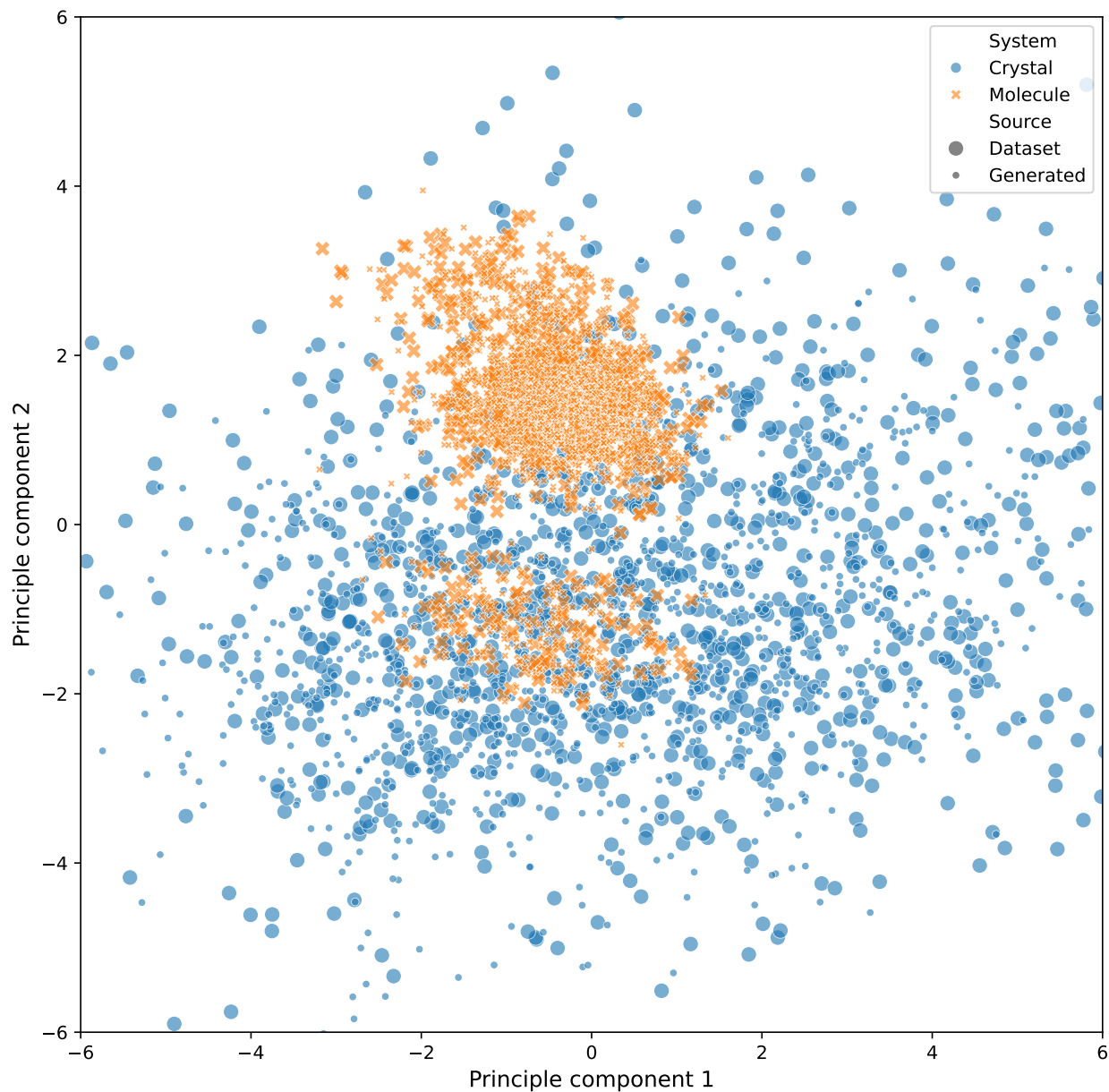


Figure 8 PCA plot of latent embeddings from ADiT's VAE for 100 data points from the MP20 and QM9 datasets, as well as 100 ADiT-generated crystals/molecules each. Each point represents an atom, coloured by the system type and sized by whether it comes from real data or generated latents. **The joint latent space shows distinct clusters between molecules and crystals, with tighter clustering for molecules and more spread for crystals, reflecting the greater diversity of elements and local geometric environments in periodic crystal structures.**

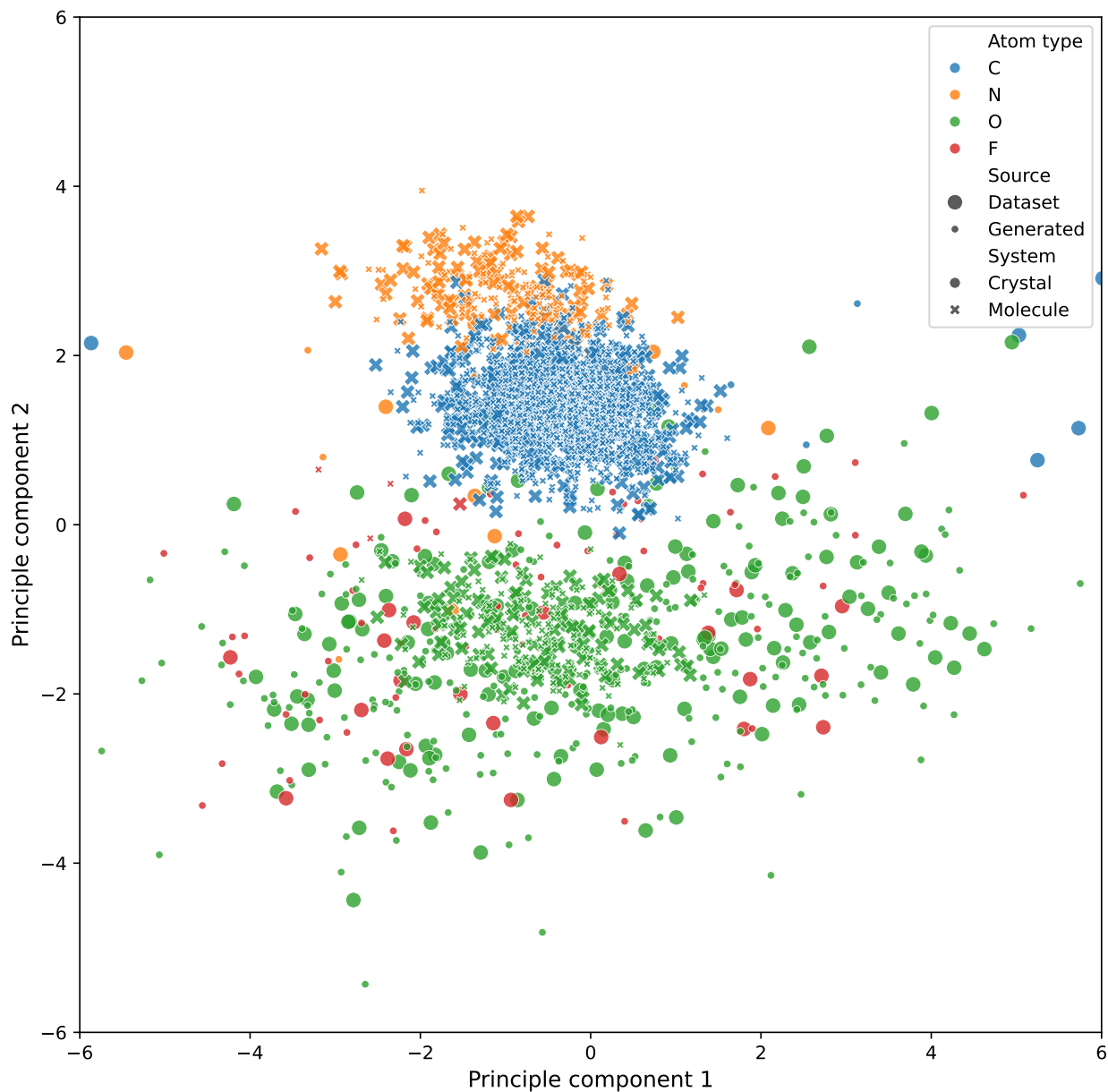


Figure 9 PCA plot of latent embeddings for carbon, nitrogen, oxygen, and fluorine atoms from ADiT’s VAE for 100 data points from the MP20 and QM9 datasets, as well as 100 ADiT-generated crystals/molecules each. Each point represents an atom, coloured by atom type and sized by whether it comes from real data or generated latents. Principle component 1 visually correlates with whether a system is a molecule (within range $-2 - 2$) or crystal. Principle component 2 visually correlates with the atom type. **The joint latent space shows distinct clusters for different atom types, with oxygen atoms having similar representations in both molecules and crystals. This overlap in oxygen atom representations suggests that ADiT’s latent space captures shared chemical properties across periodic and non-periodic systems, enabling effective knowledge transfer during joint training.**

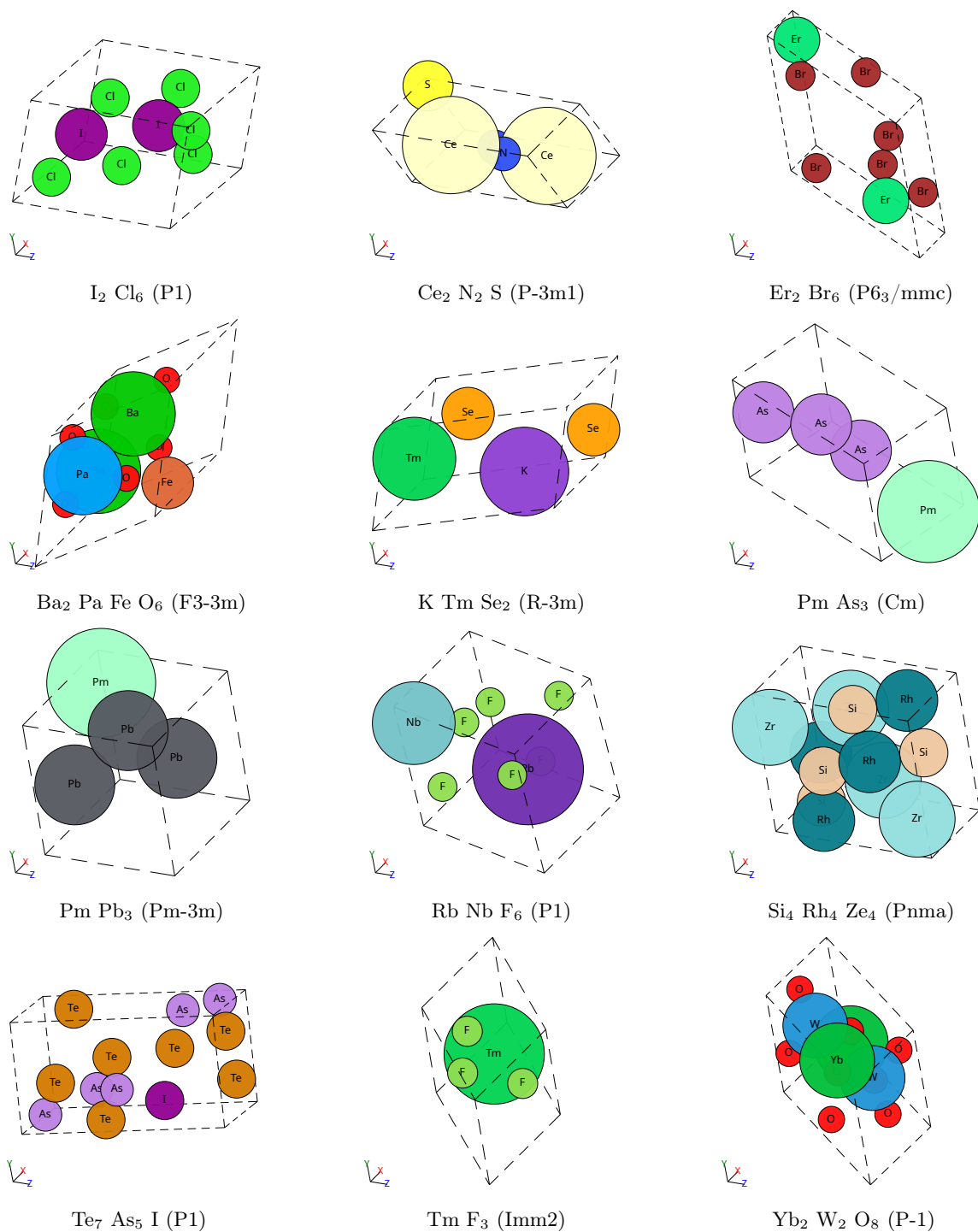


Figure 10 Generated crystals from ADiT trained jointly on MP20 crystals and QM9 molecules.

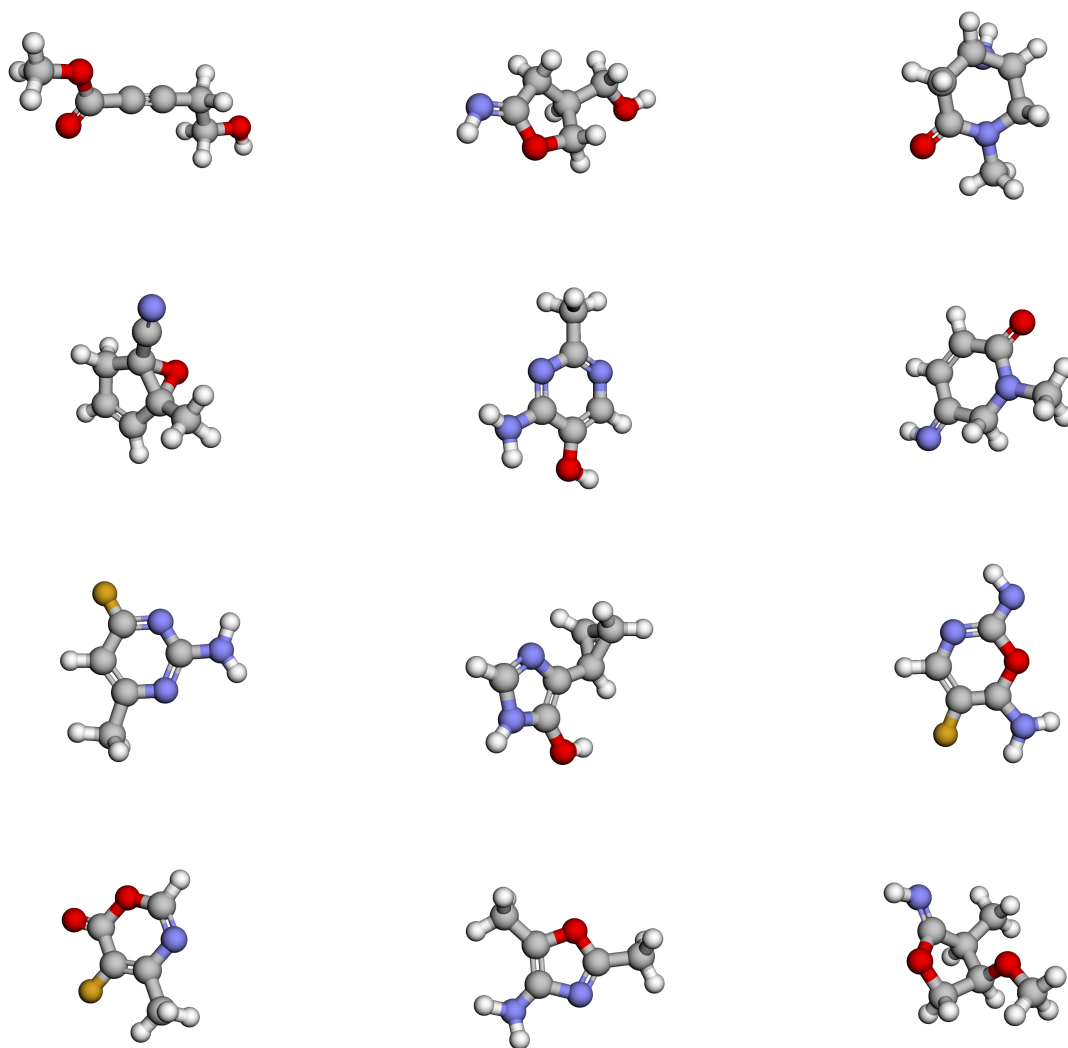


Figure 11 Generated molecules from ADiT trained jointly on MP20 crystals and QM9 molecules.

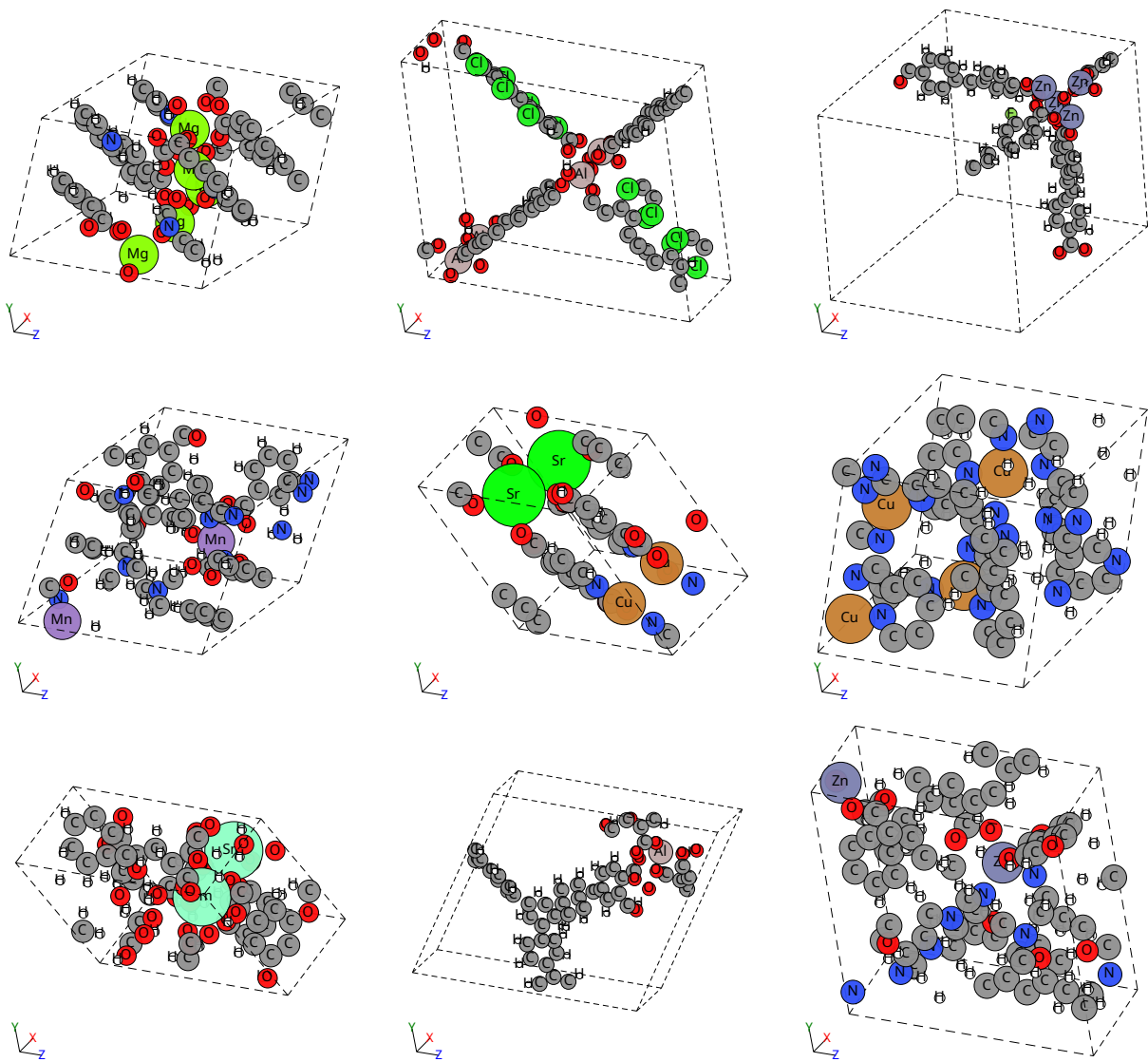


Figure 12 Generated metal-organic frameworks from ADiT trained jointly on QMOF150 metal-organic frameworks, MP20 crystals and QM9 molecules.